catalysts

MDPI

Review

Graphitic Carbon Nitride-Based Photocatalysts for Uranium Reduction and Extraction: From Fundamentals to Applications

Zhenling Zhao [1], Xuehong Yuan [2,*], Shuzhao Pei [3] and Sai Zhang [1,*]

[1] College of Chemistry and Life Science, Beijing University of Technology, Beijing 100124, China; zzl0234@emails.bjut.edu.cn
[2] Faculty of Chemical Engineering and Energy Technology, Shanghai Institute of Technology, Shanghai 201418, China
[3] State Key Laboratory of Urban Water Resource and Environment, School of Environment, Harbin Institute of Technology, Harbin 150090, China; sz.pei@hit.edu.cn
* Correspondence: yuan@sit.edu.cn (X.Y.); zhangsai92@bjut.edu.cn (S.Z.)

Abstract

Nuclear energy has become a promising substitute for traditional fossil fuels (e.g., coal, oil, and natural gas) by reason of its ultra-high energy density, firm power generation, and near-zero carbon emissions. However, the shortage of uranium resources is threatening the sustainable development of nuclear power, and meanwhile the nuclear fuel front-end cycle inevitably causes radioactive uranium-bearing wastewater discharge, resulting in severe environmental pollution. Nowadays, the extraction and enrichment of uranium in seawater and uranium-containing wastewater offer a prospective avenue to secure the long-term viability of nuclear power with environmental conservation. Among numerous strategies, photocatalytic extraction of soluble hexavalent uranyl (U(VI)) over graphitic carbon nitride (g-C_3N_4), a conjugated polymer semiconductor, is increasingly attracting widespread attention due to its high solar energy utilization, environmental friendliness, high selectivity, good stability, and low cost. A comprehensive overview that pinpoints research directions for novice researchers is urgently required. Herein, the development progress of g-C_3N_4-mediated photocatalytic U(VI) extraction is briefly introduced. Subsequently, the possible mechanisms are discussed with the assistance of advanced characterization techniques, and the influential factors for catalytic efficiency are also discussed. Moreover, multiple applications of g-C_3N_4-based catalysts on photocatalytic U(VI) reduction and extraction are elaborated, especially for modularization approaches on a large scale. At length, the future challenges and prospects in photocatalytic uranium extraction from water bodies are proposed. This review aims to offer fundamental insights into designing and exploring novel g-C_3N_4-based photocatalysts for soluble U(VI) enrichment in water bodies, especially opening up new avenues for the future development of sustainable uranium extraction technologies in practice.

Keywords: uranium; g-C_3N_4; heterogeneous photocatalysis; extraction; water environment

Check for updates

Academic Editor: Roberto Fiorenza

Received: 31 January 2026
Revised: 26 February 2026
Accepted: 4 March 2026
Published: 6 March 2026

Copyright: © 2026 by the authors. Licensee MDPI, Basel, Switzerland. This article is an open access article distributed under the terms and conditions of the Creative Commons Attribution (CC BY) license.

1. Introduction

Natural uranium, one primary raw material for the nuclear fuel cycle, has been regarded as an irreplaceable strategic resource worldwide [1]. To pursue carbon peaking and carbon neutrality goals, the demand for uranium resources is sharply increasing. Meanwhile, the scarcity of uranium ore resources, together with the inevitable generation of uranium-bearing wastewater during nuclear fuel front-end cycles, severely threatens

sustainable nuclear power development [2]. Generally, uranium species mainly exist as soluble hexavalent uranyl (U(VI)) in natural aerobic water environments, which are easily transformed into immobile precipitation under an anaerobic environment or in the presence of rich carbonate ions (HCO_3^-) [3,4]. Uranium is abundant in seawater, with a total amount of 4.5 billion tons, which is 1000 times higher than that in traditional mineral deposits [5]. Therefore, the immobilization and extraction of U(VI) from seawater and wastewater offer a feasible strategy to achieve sufficient uranium resources for future nuclear energy development. Traditional uranium extraction technologies include ion exchange, adsorption, chemical precipitation, and solvent extraction, which commonly suffer from poor selectivity, sluggish reaction kinetics, secondary pollution, and high operation costs [6]. Heterogeneous photocatalysis, as an emerging technology, is drawing widespread attention for U(VI) reduction and extraction in the past decade due to the sustainable harnessing of renewable solar energy [7].

In general, the photocatalytic extraction of uranium from water bodies involves adsorption, photoreduction of soluble U(VI) to insoluble U(IV) species, and photo-deposition processes. To develop photocatalytic extraction technology, the crucial core lies in designing and constructing highly efficient photocatalysts [4]. As a typical polymer semiconductor, graphitic carbon nitride (g-C_3N_4) has been widely studied and exhibits enormous potential in soluble U(VI) extraction via photocatalysis due to its low cost, visible-light response, facile preparation, and easily tailored structure [8,9]. In addition, the conjugated polymer structure with van der Waals interactions and metal-free characteristics determines its high stability and the prevention of secondary pollution [10]. Notably, nitrogen vacancies are easily generated in the heptazine skeleton, which introduce defect levels and provide low-coordinated C atoms as Lewis acid sites to preferentially coordinate with the equatorial oxygen of uranyl, thereby enhancing the adsorption of U(VI) species [11]. The "soft" coordination pockets are also easily created, with highly delocalized π electrons and N lone pairs, which form σ-π cooperative bonds with the 5f/6d orbitals of U(VI) to provide a rapid electron transfer channel [4,12]. As previously reported by Wang et al., a nitrogen-rich carbon nitride polymer (C_3N_5) was successfully engineered by connecting triazine units with azo bridges for efficient U(VI) extraction [13]. Benefiting from the enlarged conjugation degree, the adsorption capacity of C_3N_5 towards U(VI) species was significantly increased in contrast to primary g-C_3N_4 (Figure 1A), and the enhanced π-π^* transition also boosted charge carrier transfer for high-performance photocatalytic U(VI) extraction. Superior to conventional photocatalysts (e.g., TiO_2 and ZnO) and cutting-edge materials (e.g., COFs and MOFs), the comprehensive advantages of g-C_3N_4 materials endow themselves with the underlying potential for future industrialization and large-scale practical applications [14].

In comparison, primary g-C_3N_4 photocatalysts are usually faced with inherent limitations, including the weak visible-light response, small specific surface area, insufficient active sites, easy charge carrier recombination, high transport resistance from stacked layered structure, and low mass transfer [15]. Various modification approaches are successively explored to optimize the photoelectric performance and surface properties, such as morphology control, element doping, heterostructure construction, defect engineering, and so on [16]. For instance, Wang et al. introduced tunable mesopores into g-C_3N_4 to create MCN photocatalysts with high surface-to-volume ratios. The optimized MCN1.0 with the highest specific surface area and largest pore volume (191 m^2/g and 52.1 cm^3/g) exhibited the best photocatalytic reduction behavior for U(VI), with an extraction rate of 2.99 g/g [17]. To expand the visible-light response and increase the active sites, Zhang et al. synthesized O, P co-doped g-C_3N_4 (OPCN) by a facile one-step thermal polycondensation with the mixture of melamine and melamine polyphosphate [18]. In addition, a series of S-scheme ZISCN heterojunctions were also prepared by Dai et al. with excellent uranium

extraction, of which ZISCN-2 showed an obviously improved U(VI) extraction efficiency than individual g-C_3N_4 and $ZnIn_2S_4$ [19]. Li et al. introduced an O-vacancy C_3N_4-CeO_{2-x} (CN-CeO_{2-x}) heterostructure for effective U(VI) removal in organic radioactive wastewater [20]. The O vacancies on the surface of g-C_3N_4, being shallow traps, could effectively accumulate photoelectrons and inhibit charge carrier recombination in the CN-CeO_{2-x} composites, thereby prolonging the charge lifetime and accelerating subsequent active species generation during reactions. Efficacious modification strategies offer unprecedented opportunities for g-C_3N_4-based materials as the next-generation photocatalysts to acquire uranium resources from water bodies, thereby establishing innovative and green-oriented paths for sustainable nuclear energy utilization.

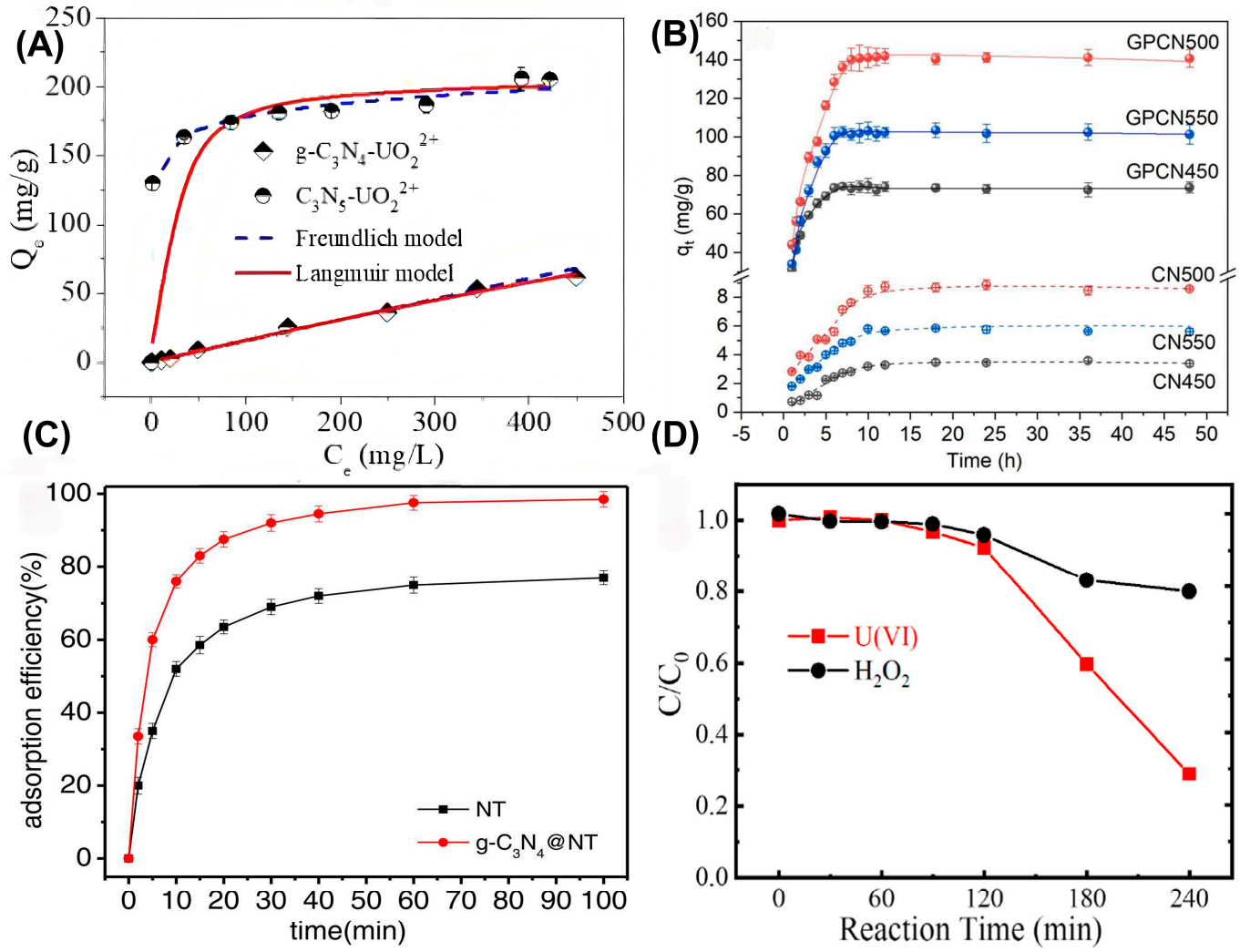


Figure 1. (**A**) Comparison of adsorption performance of uranium by g-C_3N_4 and C_3N_5, adsorption isotherms for U(VI). Reprinted with permission from ref. [13]. (**B**) Effects of contact time on the sorption of U(VI). Reprinted with permission from ref. [21]. (**C**) Effect of reaction time on the U(VI) adsorption of g-C_3N_4 @NT and NT. Reprinted with permission from ref. [22]. (**D**) Homogeneous reaction between U(VI) and H_2O_2. Reprinted with permission from ref. [23].

Over the last few years, numerous interesting and significant findings on g-C_3N_4-based materials concerning uranium enrichment have been rapidly reported, and a comprehensive overview of g-C_3N_4 photocatalysts for superior U(VI) extraction with future prospects is urgently needed. In this review, the recent advances and conceptual framework of photocatalytic U(VI) reduction and extraction are introduced, containing the research background, reaction kinetics, extraction mechanisms, advanced characterization techniques,

and interfering factors. Diverse applications and modularization design at the industrial level are then presented for better understanding. At last, a critical outlook on the opportunities and challenges in the exploration of efficient g-C_3N_4-based catalysts, the construction of a photocatalytic system, and their applications at a large industrial scale are presented, offering strategic guidelines for the rational design of g-C_3N_4-based materials to achieve soluble U(VI) enrichment from aerobic water environments.

2. Basic Principles of g-C_3N_4-Based Photocatalysts for U(VI) Reduction and Extraction

2.1. Possible Mechanisms and Kinetics of Photocatalytic U(VI) Reduction and Extraction

The photocatalytic immobilization of soluble U(VI), especially for the coupled adsorption–photocatalysis process, has been systematically explored in recent years. Generally speaking, the entire process of the photoreduction of U(VI) from water bodies involves adsorption, reduction, and deposition processes, which require unique morphological and crystallographic features (e.g., a multi-dimensional porous structure and flower-like morphology), plentiful active sites, and appropriate band alignment [16]. Thus, ion diffusion, mass transfer and the surface adsorption of U(VI) species are promoted, which are beneficial for enhancing the photoreaction kinetics of U(VI) immobilization, with simplified solid-liquid separation and catalyst regeneration. This process was verified by Dhanasekaran et al. with g-CNA as the target catalyst through a batch thermodynamic experiment, which found that U(VI) was enriched onto g-CNA by electrostatic interaction with a monolayer adsorption [24]. As for photoreduction, g-C_3N_4-based catalysts are excited by light irradiation with electron transition from the valence band (VB) to conduction band (CB), and then photoelectrons can directly reduce U(VI) to U(IV). In addition, indirect immobilization of U(VI) also occurs by reacting with intermediate reactive species, such as H_2O_2 and hydroxyl radical ($^{\bullet}OH$), to form sparingly soluble precipitates on the catalyst surface. It should be noted that the uranium-bearing intermediates and final products are governed by reaction pathways, including surface electron transfer, single- or double-electron transfer, and adsorption–reduction synergy effects, which collectively constitute an integrated mechanistic paradigm of "adsorption–activation–reduction immobilization". Most importantly, surface adsorption plays a decisive role in the photocatalytic process. Firstly, surface adsorption is usually deemed as the rate-controlling step due to the trigger mechanism from close contact of U(VI) species with catalysts. Also, good spatial consistency between the adsorption and catalytic site is crucial, which can effectively suppress quantum losses. For example, Yang et al. utilized a surface functionalization method to decorate phosphorus-containing groups onto g-C_3N_4 (GPCN), and thus boosted U(VI) ion capture from an aqueous solution [21]. As shown in Figure 1B, the adsorption capacity of GPCN500 with phosphate groups was significantly improved due to its effective interaction with U(VI) by forming uranyl hydrogen phosphate, eventually achieving excellent catalytic performance in contrast to pure CN. Considering the strong coordination ability between phosphorus groups and U(VI) ions, Yang et al. further prepared a phosphorus-modified g-C_3N_4 (PCN) to reduce and extract U(VI) from an aqueous solution in 2025 [25]. Clearly, the visible-light absorption of PCN was enhanced after P incorporation, which exhibited excellent photocatalytic performance for U(VI) reduction. Experimental results proved that U(VI) species were favorably coordinated onto the surface of PCN by forming a complex with the elongated U=O bonds, on the basis of a surface adsorption–catalysis synergy effect, and subsequently the photoelectrons in the catalysts directly reduced U(IV) and subsequently hydrolyzed U(IV) species into uranium oxides in situ, during which phosphate-binding sites were synchronously dissociated and regenerated for further reactions. In this study, the team led by He compared the fitting effects of

the pseudo-first-order and pseudo-second-order kinetic models on the adsorption data of U(VI) on PCNs. They found that the pseudo-second-order model was more suitable (with a higher correlation coefficient), indicating that the adsorption process was mainly controlled by chemical adsorption rather than the pseudo-first-order kinetic behavior dominated by physical adsorption. Dynamics studies have shown that the effective separation and transmission of photogenerated electrons are the key factors determining the reduction rate. Phosphorus modification enhances the adsorption affinity of the material for U(VI) and its visible-light absorption ability, thereby accelerating the photocatalytic reduction reaction process. Moreover, the cyclic experiments revealed that the PCNs maintained 80.3% of the initial rate after five cycling tests, verifying their kinetic stability. Moreover, Wang et al. found that UO_2^{2+} was easily reduced into UO_2^{+} in the presence of organic substances under visible-light irradiation, and then converted into uranyl peroxide by reacting with H_2O_2 in an aerobic environment [23]. However, the invalid consumption of photoelectrons occurred unavoidably, along with side reactions, and then U(IV) was re-oxidized into U(VI), as illustrated in Figure 1D. Four possible strategies have been proposed to suppress these side reactions and maintain high reduction activity in the photocatalytic process, including selective adsorption control, energy level regulation, surface coordination engineering, and the establishment of interfacial electric field, eventually achieving efficient U(VI) extraction with a high electron utilization rate and offering a viable pathway toward practical engineering applications [12].

2.2. Advanced Techniques for Catalytic Characterization

As is commonly known, characterization techniques play a very important role in investigating the catalytic mechanism of photoreduction and the extraction of soluble uranium species. The mechanisms of site binding and electron transfer involved in different uranium extraction processes share commonalities. These commonalities can be captured by characterization methods and then used to accurately analyze specific mechanisms. Different characterization methods provide strong evidence for in-depth exploration of the mechanisms. The combination of multiple advanced characterization methods contributes to comprehensively analyzing structure–activity relationships and reaction kinetics, involving surface adsorption, the chelation effect, charge carrier transfer, reduction path, and the immobilization process of U(IV) species, thereby providing an atomic-level mechanism for the precise design of efficient and stable photocatalysts for sustainable uranium extraction, as previously reported, A. Dhanasekaran et al. successfully extracted hydroxyapatite from eggshell bio-waste and embedded it into diethylene glycol acid-functionalized g-C_3N_4 to obtain a desired HAp@D-gCN nanocomposite for U(IV) extraction [26]. The composition, morphology and surface properties of HAp@D-gCN were evaluated by combining SEM, TEM, XRD, BET, FTIR and zeta-potential measurements. As shown in Figure 2A, the successful extraction of U(VI) onto HAp@D-gCN was confirmed by FTIR measurement after the reaction. The phosphate group stretching vibration peak in the 966–1120 cm^{-1} range of the FTIR spectrum proved the successful synthesis of hydroxy-apatite. The peaks at 1630 cm^{-1} (C=O stretching vibration) and 1020 cm^{-1} (C-O-C stretching vibration) indicated that diethylene glycol acid (DGA) was successfully grafted onto the surface of g-C_3N_4, providing chelating sites for uranium adsorption. The aromatic C-N/C=N stretching peaks in the 1250–1504 cm^{-1} range confirmed the presence of graphite-like carbon nitride. The characteristic peak shift in the FTIR spectrum after adsorbing U(VI) proved that the corresponding groups participated in the coordination of U(VI), accompanied by the appearance of characteristic peaks at 996 cm^{-1} (U=O stretching) and 490 cm^{-1} (O-U-O bending), directly confirming the adsorption of uranium anions on the material's surface. The FTIR results support the cooperative mechanism of ion exchange and surface complexation in

the study. In situ DRIFTS is mostly used to track the changes in surface acid–base sites and energy bands during catalytic activation, while in situ EXAFS was performed to determine the coordination configuration between U species and catalysts. For example, Hu et al. prepared a novel amidoxime/g-C_3N_4 (AO/g-C_3N_4) to capture U(VI) from various water conditions [27]. As observed in Figure 2B,C, the capture behavior of U(VI) onto AO/g-C_3N_4 through surface complexation was confirmed by EXAFS and XPS analysis. In XPS, the U 4f high-resolution spectrum did not detect the U(IV) signal, which proved that no reduction reaction of U(VI) occurred during the adsorption process, confirming the pure adsorption process. In the N 1 s and O 1 s spectra, the amine oxime group shifted after adsorption, indicating that the N and O atoms in the AO group participated in the coordination of U(VI), directly proving that the AO group is the main adsorption site. At pH values of 4.0 and 6.0, the EXAFS spectra showed similar coordination structures, indicating that although the U(VI) species in the solution changed with pH, AO/g-C_3N_4 achieved efficient adsorption through stable inner-layer coordination, which was consistent with the results of the surface complexation model. The transformation of U(VI) to other lower valence states was confirmed by time-resolved in situ XAFS measurement. By combining this with in situ TEM and selected diffraction analysis, the two-step formation process of the coordination and nucleation of uranium-bearing products was discovered. After cycling tests, the used samples were then measured by in situ DRIFTS/XAFS to confirm the excellent stability and provide guidance for subsequent defect passivation strategies. Aiming to reveal the complete mechanism of charge transfer and uranyl reduction–nucleation–crystallization, fs-TAS/TRPL and operando EPR were also employed to analyze the efficient separation and migration of photogenerated charge carriers. Finally, operando Q-XAFS, time-resolved DRIFTS, and in situ TEM were employed to monitor the electron transfer-induced valence transition, nucleation dynamics, and crystallization of uranium species. This enabled the comprehensive elucidation of a complete mechanistic pathway for photocatalytic U(VI) reduction over g-C_3N_4.

Moreover, density functional theory (DFT) calculations have also been employed in analyzing and guiding the exploration of photocatalysts for specific photocatalytic reactions, through which the reaction routes, energy barriers, and structure–activity relationships observed in the experiments can be unveiled at the micro level from an atomistic viewpoint. To predict active sites, the experimental spectra can be effectively translated into geometric models, and then the adsorption criteria are offered by establishing substrate and adsorption models. Regarding reaction pathways and energy barriers, the time-scales of TRPL/Q-XAFS are converted into energy scales, and key intermediates are commonly analyzed by establishing a reduction route of the U(VI) photoreduction mechanism. By utilizing the above-mentioned results, DFT calculation gives deep insights into the electronic structures of the catalysts, during which operando EPR signals are translated into orbital images for PDOS docking and hole capture. In a word, the entire reaction process is simulated using different computational approaches, including the adsorption energy, reaction energy barriers, PDOS, and reaction dynamics, enabling the extraction mechanism of U(VI) onto g-C_3N_4 to be understood more clearly. In 2018, Zhang et al. prepared a novel porous g-C_3N_4 using urea and natural crab shells as the precursor and biological template, respectively, through a facile thermal polymerization method [28]. Multi-scale characterization methods confirmed that porous g-C_3N_4 was successfully synthesized, with the introduction of a porous structure and increased specific surface area. Integrating EXAFS results and DFT calculations (Figure 2D), the adsorption mechanism of inner-sphere surface complexation was proved between uranyl and g-C_3N_4, with a strong interaction. The results showed that porous g-C_3N_4 exhibited a high uranium adsorption capability and strong binding ability. In addition, Chen et al. reported a novel hollow boron carbon nitride

nanotube (BCN-HNTs) with tunable p-n homojunctions as a metal-free photocatalyst for efficient uranium extraction [29]. Combing DFT calculations with other spectroscopic analyses, hexagonal carbon rings were verified to be introduced into h-BN and tunable p-n homojunctions were formed. It was found that the introduction of C atoms into the h-BN lattice increased the adsorption energy of uranium, thereby enhancing the uranium extraction capacity (Figure 2E–H). Nowadays, machine learning is also increasingly applied to guide the design and application of photocatalysts, including mapping the "active-site fingerprints" to catalytic activity one-by-one through specific strategies. The utilization of machine learning can encode the atomic arrangement and electronic structure into 830-dimensional active-site fingerprints, and establish a direct mapping with the experimental reduction half-life using GBR. Then, SHAP is applied to analyze the charge transfer and local disorder for the activity sources in a reverse direction. Eventually, the reverse visualization design of the "active site-color relationship" is achieved to guide the construction of photocatalysts.

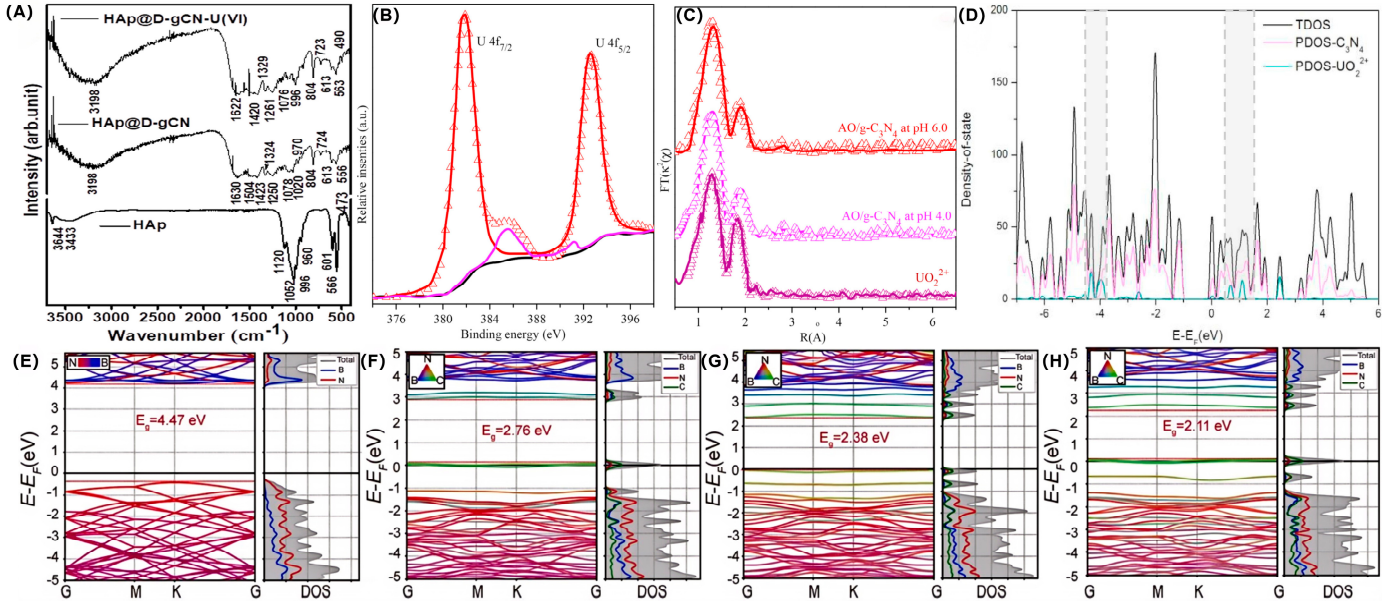


Figure 2. (**A**) FTIR spectra of HAp and HAp@D-gCN nanocomposites. Reprinted with permission from ref. [26]. (**B**) XPS and (**C**) EXAFS analysis of U(VI) capture on AO/C_3N_4, pH = 4.5, m/v = 0.1 g/L, T = 298 K. Reprinted with permission from ref. [27]. (**D**) Calculated density of state of g-C_3N_4/uranyl complexes. The black line represents the total DOS (TDOS), and the pink and green ones represent the partial DOS (PDOS) of g-C_3N_4 and UO_2^{2+}, respectively. Reprinted with permission from ref. [28]. (**E**–**H**) Calculated band structures and corresponding density of states for $B_{25}N_{25}$ and $B_xN_yC_z$ models. Reprinted with permission from ref. [29].

2.3. Interfering Factors for U(VI) Removal from Water Matrices

The efficiency, selectivity and catalytic stability of g-C_3N_4-based photocatalysts in extracting uranium from uranium-containing wastewater and seawater are jointly affected by multiple factors, including the surface chemistry, physical structure, solution chemistry and light conditions. In general, unique surface properties, such as functional groups, specific morphologies and a porous structure, directly affect the behaviors of U(VI) extraction with g-C_3N_4-based photocatalysts. The introduced functional groups, like the cyano, carboxyl and phosphate groups, usually serve as coordination sites for U(VI) species, and also regulate the electric energy level for efficient separation of charge carriers, consequently enhancing the complexation ability and photoreduction activity. By creating superior apparent morphology and adequate surface pores, g-C_3N_4-based materials endow

the specific surface area with the sufficient exposure of active sites and rapid mass transfer in the reaction system. Additionally, the initial solution pH is also vital, which decides the form of U(VI) species that exists in the solution. Commonly, U(VI) mainly exists as the UO_2^{2+} species at a pH in the range of 4-10, which is easiest to capture. As confirmed by Zhang et al., an innovative single-pot method was developed to prepare a bifunctional nanohybrid material, which incorporated nano-scale zero-valent iron (NZVI) between the layers of g-C_3N_4 to isolate U(VI) from wastewater [30]. The introduction of g-C_3N_4 as the matrix effectively suppressed the oxidation of NZVI and enhanced the photocatalytic reactivity. As shown in Figure 3A, the higher pH value was conducive to the adsorption of positively charged U(VI). However, in strong acid or alkali conditions, uranyl ions were easily complexed with carbonate and hydroxide ions, with the affinity being reduced. Meanwhile, the environmental atmosphere also has a critical impact on U(VI) photoextraction. For example, Liang et al. synthesized a g-C_3N_4-supported nZVI (g-Fe) composite and found that the uranium species adsorbed onto the g-Fe composite was only U(VI) under aerobic conditions, while both U(VI) and U(IV) were adsorbed under anaerobic conditions [31]. Therefore, in an aerobic environment, adsorption rather than reduction was the main reaction route for removing U(VI) from water bodies (Figure 3B). In addition, Fu et al. designed a layered hollow core–shell-structured Bi_2O_3/g-C_3N_4 Z-scheme heterojunction photocatalyst and successfully applied it to photocatalytic uranium extraction under aerobic and anaerobic conditions, achieving extraction efficiencies of 98.4% and 99.0%, respectively [32]. Zhang et al. prepared a novel composite of CdS and nitrogen-deficient g-C_3N_4 (CdS/PCN) for the photocatalytic reduction of uranyl under aerobic conditions [33]. It was observed that CdS/PCN not only displayed a high photoreduction activity towards uranyl under aerobic conditions, but also the photo-corrosion of CdS by oxygen and h^+ was effectively inhibited. Interestingly, the removal efficiency under air conditions was superior to that in a N_2 or O_2 (30%) atmosphere, indicating that an appropriate amount of oxygen accelerated the reduction reaction, while excessive oxygen weakened the reduction behavior (Figure 3C,D). Meanwhile, excessive dissolved O_2 re-oxidized U(IV) to U(VI).

During photocatalytic processes, various competitive reactions weaken the catalytic selectivity and stability of g-C_3N_4-based materials. The most important factor is the competition of coexisting ions in complex water bodies, especially with high salinity, various cations and anions such as Ca^{2+}, Mg^{2+}, and Fe^{3+}, which probably shield the charge, block active sites or form mixed complexes with U(VI), thus decreasing the active sites on catalysts. For coexisting cations, in particular, the divalent cations will occupy the double binding sites and have small ionic radii, thus having a significant competitive adsorption relationship with U(VI), and in neutral or alkaline conditions, the divalent cations will form neutral ternary complexes with U(VI) and CO_3^{2-}, thereby inhibiting the adsorption of U(VI). Yang et al. significantly enhanced the U(VI) adsorption selectivity by using phosphate-functionalized graphite-like nitrogen-doped carbon (GPCNs) [21], The specific precipitation of the phosphate group with U(VI) forms $UO_2HPO_4{\cdot}4H_2O$, which can effectively resist most cation interference. Anions, especially CO_3^{2-} and HCO_3^- [3,4] can form stable anionic complexes $[UO_2(CO_3)_2]^{2-}$ with U(VI), thus weakening electrostatic adsorption. In 2021, Li et al. first addressed the issue of forming stable complexes between carbonates and U(VI) by introducing carboxyl groups, reducing their affinity and reduction potential and thereby inhibiting the photocatalytic reaction and limiting practical applications [3]. However, the problem of dissolved oxygen oxidizing U(IV) in actual seawater was not explored. In 2024, their team further combined carboxyl-functionalized g-C_3N_4 with CdS and loaded it onto a hydrogel [4]. By activating dissolved oxygen with CdS, they simultaneously solved the problems of oxygen inhibition and carbonate complexation, and the anti-fouling property of the hydrogel provided a solution approach for the biofouling

problem in practical applications. While, F^- anions easily bind with U(VI) to alter the uranium intermediates' form and lower the reduction potential. Despite the presence of these substrates, organic matter, such as humic acid, EDTA, etc., can chelate with U(VI) and occupy the coordination sites on the catalysts' surface, leading to a decrease in catalytic efficiency. In addition, microbial films from natural water bodies cover the active sites and increase reduction potential. To suppress the competitive reactions and enhance the anti-interference ability of complex water bodies, diverse functionalization strategies are explored for collaborative design, which eventually achieve a higher extraction rate and cycling stability for uranium enrichment in uranium-containing wastewater and real seawater, significantly improving the sustainable supply potential of nuclear resources.

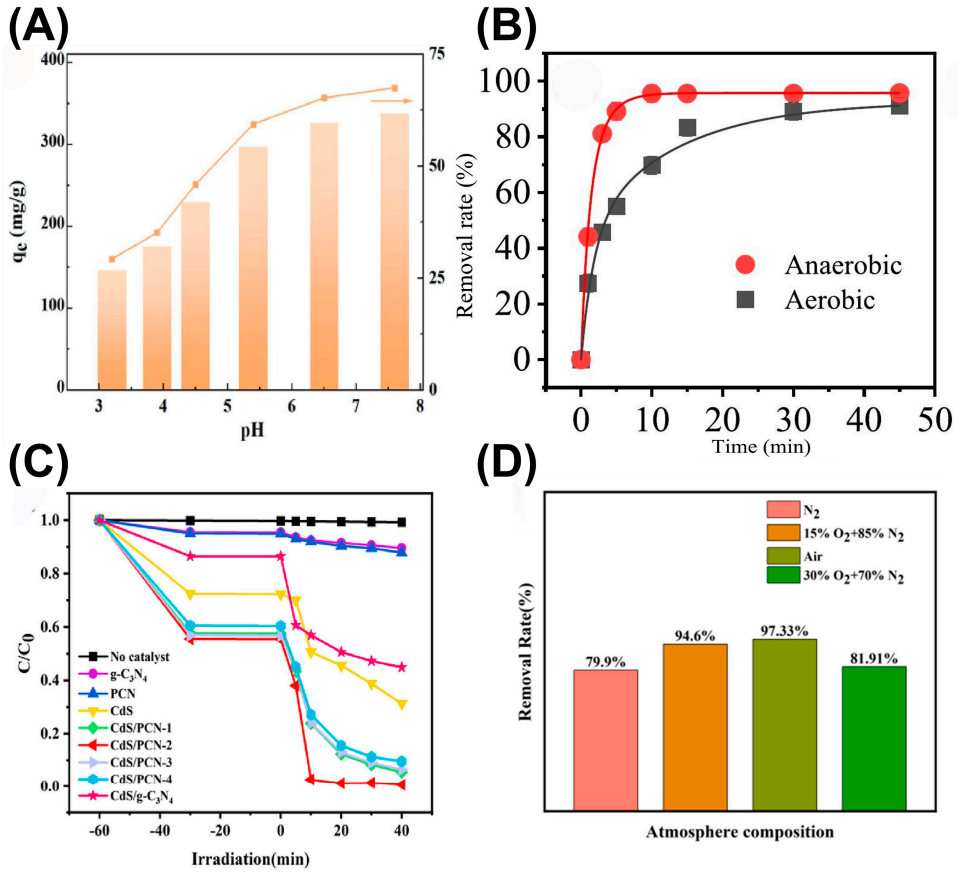


Figure 3. (**A**) Effects of solution pH on U(VI) adsorption onto g-C_3N_4/NZVI. Reprinted with permission from ref. [30]. (**B**) Effects of dissolved oxygen on the photocatalytic reduction of U(VI). Reprinted with permission from ref. [31]. (**C**) Removal efficiency of U(VI) by different photocatalysts and (**D**) effect of atmosphere conditions on the photocatalytic reduction of U(VI). Reprinted with permission from ref. [33].

3. Applications of g-C_3N_4-Based Photocatalysts for U(VI) Extraction from Water Bodies

As for photocatalytic immobilization, the adsorption process is crucial and always serves as the rate-determining step, especially in the coupled adsorption–catalysis system. The adsorption behavior of U(VI) directly depends on the amount of surface reactive sites for g-C_3N_4-based photocatalysts. Therefore, a substantial body of literature has established how to optimize the adsorption behavior during the photocatalytic process, mainly including defect engineering, element doping, morphology regulation, surface functionalization and heterostructure construction. Considering the Sabatier principle, the reaction activity of catalysts and the adsorption strength of reactants or intermediates generally have a

volcano-shaped relationship. Weak adsorption causes inefficient interaction between the reactants and catalyst surface, while in reverse, strong adsorption leads to difficult desorption and thus the occupation of the active sites, suppressing subsequent reactions. Thus, the coordinated optimization of adsorption behavior through suitable means can simultaneously promote the activation efficiency of reactants, which is the key step to obtain an efficient synergy in an "adsorption–catalysis" integrated system. For example, Zhang et al. designed and synthesized a novel phosphorus-functionalized carbon nitride (PCN) for the rapid adsorption of uranium [34]. The adsorbent reached its maximum adsorption capacity within one minute, and the adsorption efficiency exceeded 96%. Characterization results confirmed that the adsorption of uranium onto PCN-600 relied on chemical adsorption. Also, M. Dhanu and co-workers incorporated g-C_3N_4 with rich carboxyl and hydroxyl groups under the assistance of acid and hydrogen peroxide treatment [35]. The obtained oxygen-functionalized gCN was denoted as gCN-OH and analyzed by various characterization techniques. The experimental results indicated that the adsorption capacity of gCN-OH towards U(VI) was 254.1 mg/g and the equilibrium adsorption kinetics were reached within 70 min, making it a potential choice for large-scale application. Furthermore, different from the traditional method of introducing new ligands, Wang et al. proposed an innovative strategy to graft 4-phenoxyphenol (PP) onto CNC (PCN) with the injection of π electrons to activate original ligands on CN [36]. As shown in Figure 4C, the adsorption performance of CN was enhanced due to the π electrons being delocalized from PP to activate CN through the ligands.

Constructing diverse composites is an effective strategy to modify g-C_3N_4-based photocatalysts. In 2020, Ge et al. synthesized a manganese ferrite/porous g-C_3N_4 ($MnFe_2O_4$/PCN) composite [37]. Thermodynamic analysis and XPS results indicated that the adsorption was an endothermic spontaneous process, during which amino and metal–oxygen groups were involved in the complexation adsorption of uranium. These findings confirmed that the $MnFe_2O_4$/PCN composite could be used as an ideal material for adsorbing U(VI) from the aqueous solution. Meanwhile, Ding et al. constructed a well-dispersed g-C_3N_4@NT in aqueous solution by loading nano-TiO_2 (NT) onto g-C_3N_4, which was used for the separation of uranium (VI) in wastewater [22]. Due to the filling of oxygen vacancies, the redox effect and inner-sphere complexation between uranium (VI) and g-C_3N_4@NT, g-C_3N_4@NT is expected to be used for the removal of uranium (VI) from solution (Figure 1C). Similarly, Wu et al. investigated the adsorption performance of a g-C_3N_4/UiO-66 (CNUIO) composite for soluble U(VI) [38]. The coordination complexation of nitrogen-containing and oxygen-containing functional groups in CNUIO with U(VI) was responsible for U(VI) removal, thus exhibiting a maximum adsorption rate of 95.01%, which was approximately 25% and 33.73% higher than that of g-C_3N_4 and UiO-66, respectively. Surprisingly, CNUIO exhibited good reusability. In addition, Xu et al. successfully synthesized g-C_3N_4/FeS nanocomposites, in which g-C_3N_4 was used to reduce the agglomeration of FeS nanoparticles as an effective stabilizer and dispersant, thereby enhancing photocatalytic reactivity [39]. The adsorption of U(VI) by g-C_3N_4/FeS conformed better to the Freundlich model. The research results indicated that g-C_3N_4/FeS is a promising and highly efficient material for the removal of U(VI) (Figure 4A). As depicted in Figure 4B, Momin et al. successfully loaded g-C_3N_4 (GCN) onto calcined layered double hydroxides (CLDHs), and proposed a possible adsorption mechanism through Lewis acid–base interaction precipitation and surface complexation [40]. As shown in Figure 4B, the desired GCN-CLDH composite displayed a better adsorption ability for U(VI) than pure CLDH. Meanwhile, Zhao et al. proposed a simple method for preparing prussian blue-modified g-C_3N_4 and synthesized PB/g-C_3N_4 as an efficient adsorbent for U(VI) [41]. The pseudo-second-order kinetic model fitting showed that the rate constant k_2

was 0.01386–0.04095 g·(min·mg)$^{-1}$, varying with the initial concentration, and the theoretical equilibrium adsorption capacity was highly consistent with the experimental value, confirming that chemical adsorption was the main mechanism. PB/g-C_3N_4 exhibited the advantages of low cost, environmental friendliness, easy synthesis, high performance and strong stability, thus serving as a promising material for uranium-containing wastewater treatment. Also, Fang et al. decorated magnetic $ZnFe_2O_4$ (ZFO) nanospheres onto g-C_3N_4 (CN) nanosheets by direct mixing and calcination to obtain a heterostructure composite [42]. The fitting result from the quasi-second-order kinetic model (K_2 = 0.0006 g·(mg·h)$^{-1}$) indicated that chemical adsorption was the rate-determining step, and the strong interaction between the material and U(VI) inhibited the desorption process, thereby prolonging the usage life of the as-obtained material. During adsorption, the potential reaction mechanism was determined to be electrostatic interaction and intra-ball surface complexation, mainly attributed to Zn-O and Fe-O bonds. Also, the introduction of a magnetic substrate contributed to solving the problem of sustainable recovery for traditional materials. This not only introduced an effective strategy for preparing new magnetic adsorbents, but also provided new insights into the elimination of U(VI), which was of great significance for environmental protection and sustainable development (Figure 4D).

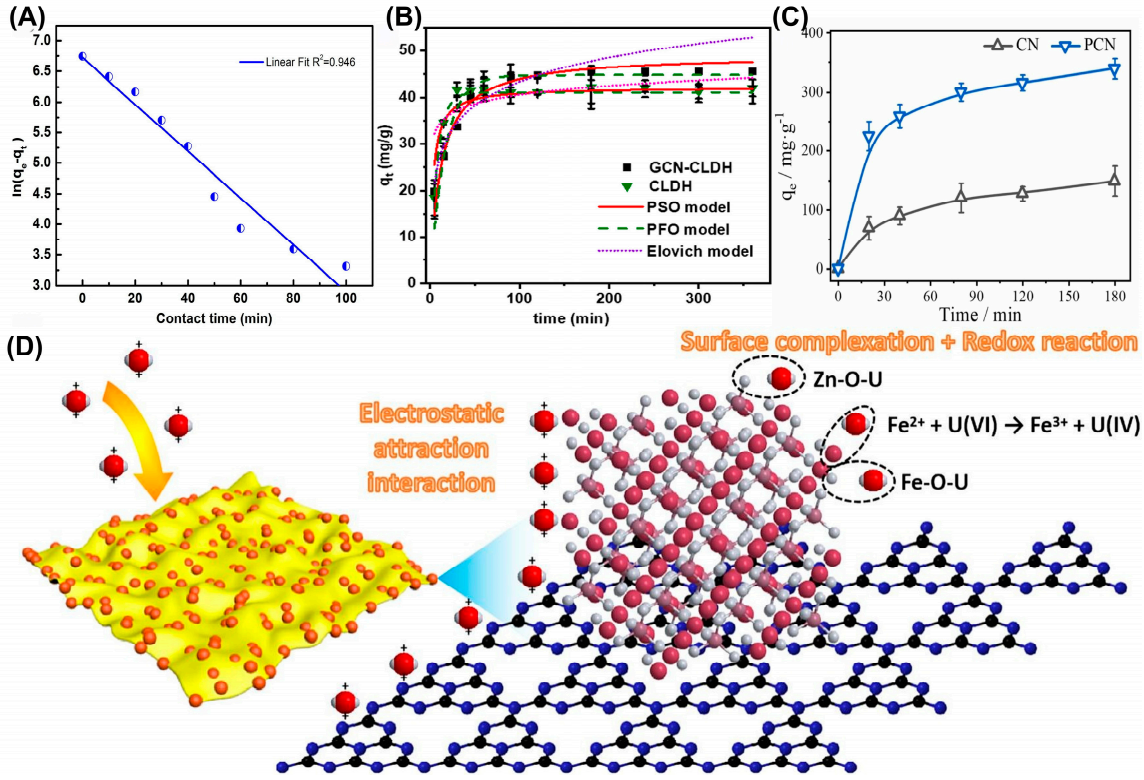


Figure 4. (**A**) Adsorption capacity of U(VI) by g-C_3N_4/FeS as a function of a pseudo-first-order kinetic model. Reprinted with permission from ref. [39]. (**B**) Kinetic effect of U(VI) on GCN-CLDH (pH = 4, dose= 0.5 g/L, and T= 298 K). Reprinted with permission from ref. [40]. (**C**) Adsorption kinetics of CN and PCN. Reprinted with permission from ref. [36]. (**D**) The possible U(VI) adsorption mechanisms of ZFOCN at pH = 5.0. Reprinted with permission from ref. [42].

Moreover, one of the most attractive approaches for modifying g-C_3N_4 is to design and construct a nanostructure. Li et al. prepared porous g-C_3N_4 by etching with HCl derived from NH_4Cl. The photocatalytic extraction performance of uranium by the gas–plastic method was 4.8 times higher than that of bulk g-C_3N_4 [43]. While, Wang et al. regulated the photocatalytic efficiency of g-C_3N_4 by introducing tunable mesopores [17]. The mesoporous g-C_3N_4 samples (MCNr, where r represents the initial mass ratio of silica to cyanamide

in the synthesis process) showed a higher specific surface area and larger pore volume. Compared with the original g-C_3N_4 (BCN), the light utilization rate and the separation efficiency of photogenerated carriers of MCN_r were significantly improved. MCN_r exhibited the enhanced photocatalytic performance for U(VI) reduction under visible-light irradiation. Furthermore, Liu et al. reported a sunlight-driven photocatalytic-assisted extraction (SUPER) method using a bifunctional carbon nitride material (CN550) [44]. By overcoming the influence of electrostatic repulsion, the adsorption capacity is no longer limited by the number of adsorption sites. Compared with g-C_3N_4, the adsorption capacity and photocatalytic activity of the obtained CN550 sample increased more than 10 times. This novel SUPER method effectively modified pristine g-C_3N_4 with stable and rapid kinetic characteristics under natural light conditions, benefiting for future application in seawater. Santiago-Aliste et al. prepared a novel nano-carrier (NCs) of g-C_3N_4-chitosan oligomer (g-C_3N_4-COS) by crosslinking with methacrylic anhydride (MA) [45]. The average particle size of the new NCs was 85 nm, with a dispersion index of 0.25. It possessed photocatalytic activity (related to the graphitic phase-like carbon nitride fragments), enzymatic degradation sensitivity (owing to the presence of COS fragments), high encapsulation efficiency (>95%) and medium-high release efficiency (>74%). The visible-light-driven photocatalytic activity of the NCs was demonstrated by reducing U(VI) to U(IV). To achieve better charge carrier separation, Li et al. synthesized a hollow tubular D-A organic semiconductor photocatalyst composed of triazine (acceptor) and carbocyclic (acceptor) structures using sodium alginate and melamine as raw materials [46]. The addition of the carbocyclic structure enables the g-C_3N_4 to have a unique hollow hexagonal tubular morphology, regulates the electron excitation model, reduces the exciton dissociation energy, and promotes the adsorption and activation of O_2. Therefore, the D-A structure established an efficient photocatalytic system for efficient uranium separation under LED light even at high concentrations of anion and cation interferences. More importantly, an innovative photocatalytic-induced uranyl coordination reaction (PIUCR) mechanism was proposed, which emphasized that the formation rate and pathway of the crystal nucleus were the most critical steps in the surface reaction of photocatalytic uranium separation (Figure 5A,B). Liu et al. reported a tunable carbon nitride nanostructure synthesized by molten salt, of which the adsorption capacity and photocatalytic activity were adjusted by varying the synthesis temperature [47]. The nanostructure of the carbon nitride obtained at 600 °C (CN600) exhibited the highest photocatalytic-assisted extraction capacity (1387.0 mg/g), which was 51 times higher than that of g-C_3N_4. Wu et al. successfully prepared crystalline carbon nitride (CCN) catalysts at different temperatures, which enhanced the efficiency of photocatalytic uranium reduction [48]. The increased crystallinity of the material improved the efficiency of electron-hole separation. Compared with bulk carbon nitride, the efficiency of photocatalytic uranium reduction was increased by 2.5 times. Meanwhile, Dang and coworkers prepared a series of nitrogen-rich carbon nitrides with different nitrogen contents and catalytic performances [49]. As the pyrolysis temperature increased, the nitrogen content continuously decreased. The triazine rings, tetrazine rings and azo bonds generated at low pyrolysis temperatures were gradually replaced by heptazine rings and single nitrogen bonds. The nitrogen-rich carbon nitride synthesized at 550 °C had the best reduction activity for U(VI) due to its good cavity structure, narrow light absorption bandgap and high electron transfer channel. Liu et al. strategically modulated the structure of polymerized carbon nitride to promote the N-doping state, thereby facilitating the enrichment of delocalized electrons [50]. Free radicals were easily generated due to the activation process from surface active sites, thus accelerating the selectivity of U(VI) reduction. Inspired by the previous work, Song et al. proposed a novel one-step method to synthesize ultrathin porous g-C_3N_4 nanosheets through microwave-assisted calcination of

urea [51]. The obtained g-C_3N_4 nanosheets presented a multi-hollow network structure with a significantly increased specific surface area. These ultrathin porous nanosheets exhibited excellent performance in reducing U(VI) to U(IV) (Figure 5C–E). Wu et al. proposed a supramolecular self-assembly strategy, using melamine and cyanuric acid as precursors, to generate carbon nitride (CN-D) through a single thermal polymerization strategy in different solvents by intermolecular hydrogen bonding force [52]. Under visible-light irradiation, CN-D could extract 98% of the U(VI) from wastewater within 60 min. After five cycling tests, the removal efficiency of U(VI) could maintain ~95%, demonstrating excellent recyclability and reusability. In addition, Zhang et al. synthesized silica photonic crystal templates by a simple bottom-up self-assembly method, and then incorporated the inverse opal structure into g-C_3N_4 to prepare g-C_3N_4 photonic crystals (CNPC) [53]. The targeted CNPC exhibited a higher specific surface area, larger pore volume, and stronger visible-light response, as well as faster separation and migration of photogenerated carriers, thereby improving photocatalytic activity.

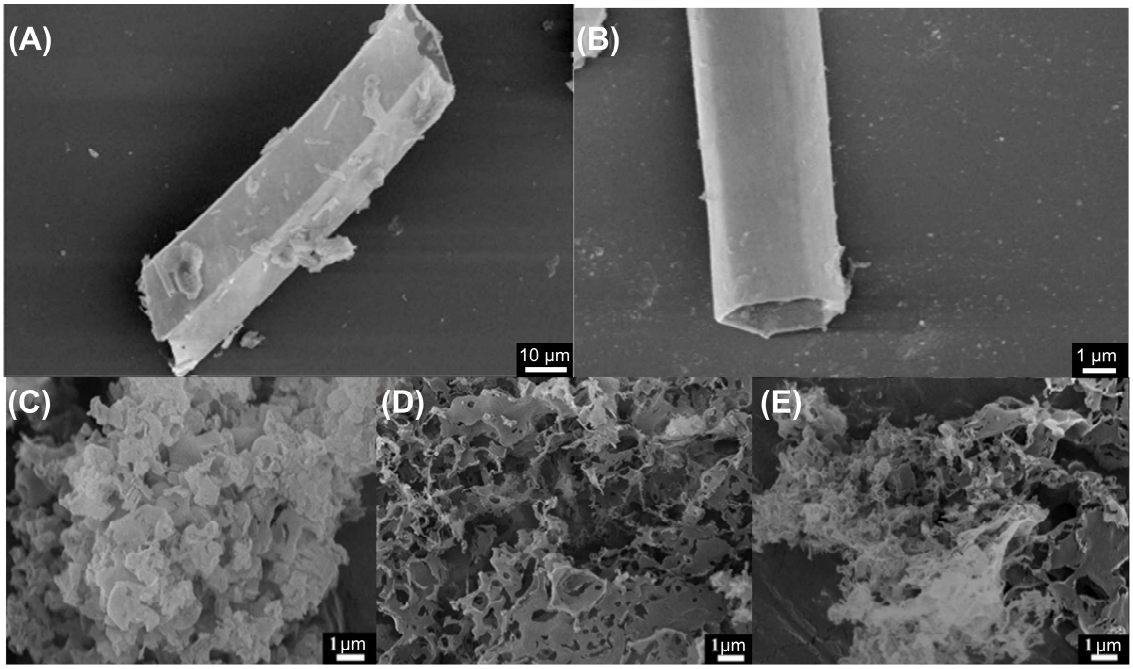


Figure 5. (**A**) The SEM images of HCN and (**B**) HCNCR. Reprinted with permission from ref. [46]. (**C**) SEM images of CN, (**D**) MCN45, and (**E**) MCN90 photocatalysts. Reprinted with permission from ref. [51].

During photocatalysis, a suitable bandgap is an important parameter considered in the design of efficient catalysts. Elemental doping is deemed a feasible strategy to regulate the electronic structure and surface properties of semiconductors, consequently improving the photocatalytic activity. Doping of metal elements is able to regulate the band structure, promote carrier separation and increase active sites, such as co-doping of sodium and potassium (Figure 6A), copper doping (Figure 6B) platinum doping (Figure 6C), and single-atom-iron-anchored g-C_3N_4 (Fe-g-C_3N_4) [54–57]. Compared with the traditional doping of Fe as modification strategy, the incorporation of single-atom Fe onto g-C_3N_4 induced a clear coordination structure, which achieved increased catalytic activity, high selectivity, and strong stability, therefore resulting in the maximum atomic utilization rate [58]. The apparent rate constant of single-atom Fe-g-C_3N_4 was 0.11177 min^{-1}, which was 82 times that of the original g-C_3N_4 (0.0056 min^{-1}) and significantly higher than that of Fe nanoparticles and doped Fe/g-C_3N_4. The single-atom Fe-g-C_3N_4 exhibited a highly efficient catalytic

performance within the solution pH range of 3.0 to 8.0, resolving the problem of the activity loss for traditional catalysts under extreme pH conditions. Non-metal-doped g-C_3N_4 mainly aims to optimize the electronic structure and enhance selectivity and is characterized by a simple process and environmental friendliness. Currently, the non-metal doping work mainly includes sulfur doping, thiophene doping, bromine doping, oxygen doping, co-doping of oxygen and phosphorus, and phosphorus doping (Figure 6D–F) [59–66].

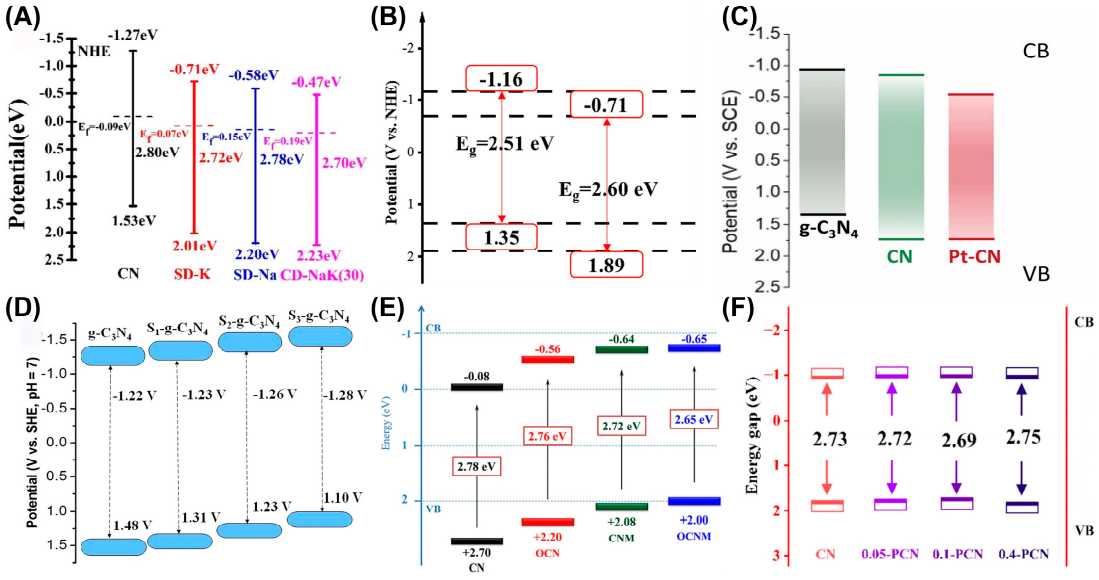


Figure 6. (**A**) Bandgap structures of CN and alkali metal-doped g-C_3N_4. Reprinted with permission from ref. [54]. (**B**) Bandgap structures of Cu-CCN-50 and BCN. Reprinted with permission from ref. [55]. (**C**) Energy band structure of g-C_3N_4, CN and Pt-CN. Reprinted with permission from ref. [56]. (**D**) Schematic electronic structure of g-C_3N_4 and S-g-C_3N_4 samples. Reprinted with permission from ref. [59]. (**E**) Band structure of CN, OCN, CNM and OCNM. Reprinted with permission from ref. [63]. (**F**) Energy band structure of CN, 0.05 PCN, 0.1 PCN, and 0.4 PCN. Reprinted with permission from ref. [65].

The construction of heterojunctions can modify the electronic structure, carrier separation efficiency and light absorption of catalytic materials. Firstly, type-II heterojunctions have been widely applied in the modification of g-C_3N_4-based catalysts. The construction of different heterojunctions has different effects on the extraction rate of uranium, as shown in Table 1. Type-II heterojunctions can achieve spatial separation of electrons and holes in different semiconductors through band alignment, reducing the electron-hole recombination rate and enhancing photocatalytic activity. For example, Chen et al. developed g-C_3N_4/graphene oxide hybrid nanosheets (g-C_3N_4/GO) as heterostructure catalysts for efficient U(VI) extraction [67]. Meanwhile, Le et al. designed and explored a homojunction into a g-C_3N_4 structure by interpenetrating a tri-triazine structure to obtain the desired ipCN catalyst, exhibiting excellent U(VI) photoreduction [68]. For better charge separation and utilization, Zhang et al. and Li et al. separately introduced flower-like MoS_2 and CdS into g-C_3N_4 by preparing MoS_2/g-C_3N_4 (FMCN) CdS/g-C_3N_4 heterojunctions to improve photocatalytic U(VI) extraction from water bodies [69,70]. To enhance the optical performance of g-C_3N_4 nanosheets (g-CNNs), Liu et al. introduced two-dimensional (2D) hexagonal SnS_2 nanosheets, which exhibited excellent U(VI) removal performance [71]. Moreover, ZnS@g-C_3N_4 (ZSGCN), MoS_2/g-C_3N_4, and MIL-100(Fe) were also coupled with g-C_3N_4 by the formation of heterojunction composites, and improved catalytic behavior for catalysts in UO_2^{2+} reduction was achieved [72–74]. In addition, Wang et al. prepared dendritic fiber-like nano-silica modified with g-C_3N_4, which was then coupled with CdS for

U(VI) photoreduction [75]. A similar sulfide, WS_2, was also grafted onto g-C_3N_4 by Wang et al. and a significantly enhanced photocatalytic performance was achieved [76]. Experimental results found that the removal rate for U(VI) reached 98% once the solution pH was adjusted to 5.0. This was attributed to the fact that the U(VI) species mainly existed in cation forms such as UO_2OH^+ and $(UO_2)_2(OH)_2{}^{2+}$ under the reaction condition, which facilitated electron transfer on the catalyst surface through electrostatic attraction. This discovery provided key process parameters for the actual treatment of uranium-containing wastewater. Liu et al. prepared the LDHS@TCN composite by an in-situ growth method [77]. LDHS@TCN maintained a high adsorption capacity within the pH range of 3 to 9. The as-obtained sample exhibited excellent activity under alkaline conditions (pH = 8), thereby overcoming the limitation of solution pH for traditional adsorbents. Apart from these, non-metallic substrates were also used to functionalize g-C_3N_4 with increased catalytic efficiencies, like GO nanosheets, organic ligands, and so on [10,78]. As reported by Hou et al., a hollow spherical g-C_3N_4 (HCN) was synthesized by a novel template method (Figure 7A) and then PTPS (PEDOT:PSS) was employed on HCN to form a donor–acceptor (D-A) heterojunction photocatalyst (PTPS@HCN) [78]. In addition, Li et al. designed and prepared a novel cyanide-modified photocatalytic material, NC-GCN/Ag_2O [79]. Kang et al. reported a general strategy of inserting a thiophene unit into the electron acceptor to form a new donor–acceptor-conjugated polymer/polymer carbon nitride heterojunction (YSS-2/CN) [80]. Peng et al. synthesized g-C_3N_4/HAP composite materials by a hydrothermal method [81]. Song et al. successfully prepared a composite material of silicon carbide and graphitic carbon (SiC_{15}@g-C_3N_4) [82]. Bismuth-based compounds were also introduced to modify g-C_3N_4 by forming efficient heterostructures (e.g., BiOI/g-C_3N_4 and Bi_2WO_6/g-C_3N_4biochar) with suitable band structures, increased visible-light response, and boosted charge transfer [83,84]. However, the limitation for U(VI) mainly lies in the sacrifice of redox potential, which leads to a weakened oxidation–reduction ability in photogenerated carriers. Schottky heterojunctions utilize the unidirectional Schottky barrier between the metal and semiconductor, with the metal side acting as an "electron sink", effectively suppressing e^--h^+ recombination. Such heterojunctions have ultra-high uranium extraction capacity and broad-spectrum tolerance, which can be constructed without a second semiconductor and have a preparation process that is easy to scale up. Therefore, Li et al. investigated the reduction effect of carbon nitride/activated carbon composite (CN/AC) on U(VI) under visible-light [16]. Wang et al. reported that nickel single atoms isolated on a sulfur-functionalized g-C_3N_4/reduced graphene oxide two-dimensional heterostructure can achieve special photoreduction of uranyl [85]. Yu et al. prepared porous few-layer C_3N_4 (PFC) by a simple bottom-up approach and combined it with Ti_3C_2 through electrostatic assembly to construct a 2D/2D heterojunction structure, labeled as TFC (Figure 7C) [1]. However, the catalytic activity was limited by the lack of light response in the metal phase, resulting in the limited utilization of sunlight, and excessive metal content can shield the active surface, causing a "shielding effect" and reducing photocatalytic activity. The Z-scheme heterojunction mimics the "Z-shaped" electron transfer route of natural photosynthesis, retaining photogenerated e^- and h^+ with efficient separation for strong redox capabilities. The Z-scheme structures feature fast uranium extraction rates and retain a strong reduction potential, which also prevents the loss of ionic mediators, and thus they are fit for complex water systems. For example, Hong et al. utilized a metal–organic framework (MOF) material containing cobalt metal as a self-sacrificing template. Through a simple thermal copolymerization, a Co-N_x coordination was successfully incorporated into g-C_3N_4, resulting in the synthesis of CoNx/g-C_3N_4 photocatalysts [86]. Some Z-scheme heterojunction composites with two suitable components have been rationally designed and constructed to efficiently extract uranyl resources from water bodies via photocatalysis,

like MoS_2/g-C_3N_4, Ti_3C_2/g-C_3N_4, $SrTiO_3$/g-C_3N_4, and WO_3/g-C_3N_4 [87–90]. In addition, Li et al. designed and prepared a novel ternary dual Z-scheme $AgVO_3$-$InVO_4$/g-C_3N_4 heterojunction (Z-AIGH) nanocomposite with a high specific surface area of 73.45 $m^2 \cdot g^{-1}$ (ZAIGH2) [91]. Under neutral conditions with a pH value of 7.0, efficient adsorption and photocatalysis were achieved, which showed a high selectivity towards common coexisting ions (e.g., K^+, Na^+, and Cl^-) and only slight interference from CO_3^{2-} and Ca^{2+}. This solved the problem of the poor stability or insufficient selectivity of traditional materials under extreme pH conditions. Under visible light irradiation, the rapid photoreduction and separation of U(VI) were realized with a removal rate greater than 98.7% within 20 min, and no organic sacrificial agents were added, thus preventing secondary pollution. This was different from the traditional photocatalytic system that relied on sacrificial agents to consume photogenerated holes, thereby enhancing the feasibility of practical applications. Inspired by a previous study, Liu et al. synthesized g-C_3N_4/Ag/TiO_2 ternary Z-scheme heterojunctions for the efficient photocatalytic reduction of U(VI) [6]. Liu et al. prepared carbon nitride nanosheets (CNNs)/UIO-66 composite materials (CNNUs) by thermal polymerization and solvothermal methods [92]. Wen et al. achieved the photocatalytic removal of U (VI) by applying a Z-scheme 2% g-C_3N_4/SnS_2-V_3/CQD1 photocatalytic system [93]. Li et al. constructed a ternary heterojunction of rare-earth indium bimetal vanadate/gC_3N_4 (MVG) by using a simple in situ self-assembly technique [94]. Qiu et al. firstly synthesized a $BiVO_4$/HCN heterojunction catalyst and successfully applied it to uranium removal with high efficiency [95]. Xiao et al. reported the synthesis and application of a Bi_2WO_6/g-C_3N_4 (BW/CN) composite material for the photocatalytic reduction of U(VI) [96]. Compared with traditional TiO_2-based catalysts that only responded to ultraviolet light (accounting for 4% of the solar spectrum), this composite material exhibited stronger light absorption in the visible-light region ($\lambda > 420$ nm), thereby expanding the spectral range during photocatalytic reaction. Through mechanism analysis, it was clearly found that $^{\bullet}O_2^-$ as an active species was mainly responsible for U(VI) photocatalytic reduction, rather than the traditional $^{\bullet}OH$. This discovery provided a new direction for designing efficient photocatalytic systems, which enhanced the reduction efficiency by regulating the generation pathway of active oxygen species on the catalyst surface. Zhu et al. synthesized CN/Ni-MOF composite materials by solvothermal method and investigated their catalytic performance for the photoreduction of uranium [97]. However, such heterojunctions are limited by the need for precise control of the thickness and defects of the interface electron mediator, otherwise it is prone to become a recombination center. Additionally, the energy-level matching window is narrow, which requires the DFT pre-screening and energy level-matched semiconductors, resulting in high experimental trial-and-error costs.

Differing from type-II and Z-scheme heterojunction, S-scheme heterojunction has received increasing attention in recent years, which is composed of two n-type semiconductors, including the reduced part (RP) and oxidized part (OP). The difference in their Fermi level induces the formation of an internal electric field and drives the directional migration of electrons Also, S-scheme heterostructures feature a flexible design, a theoretically optimal photocatalytic effect, and no need for metal or ionic mediators, thus avoiding Schottky shielding or solution phase limitations. For instance, Li et al. designed a heterojunction composite material of g-C_3N_4 and perovskite oxide (g-C_3N_4/$LaFeO_3$) (CNL5) for photocatalytic reduction of U(VI) from an aqueous solution under simulated sunlight conditions [98]. After five cycling tests, the CNL5 (a heterojunction containing 5% $LaFeO_3$) showed no significant decline in the photocatalytic reduction efficiency of U(VI), indicating its excellent structural stability and reusability. The XPS and XANES analyses revealed that U(VI) was reduced by photogenerated electrons and $^{\bullet}O_2^-$ to insoluble U(IV) (UO_2), which deposited on the catalyst surface with a removal efficiency of 74.6%. Excessive uranium

deposition might cover the active sites, but in this study, CNL5 still maintained a removal rate of 96.7% in a 0.4 mM U(VI) solution, indicating that its surface could accommodate high-concentration uranium deposition without significant passivation. Li et al. prepared MoS_2 and P-doped g-C_3N_4 nanocomposites (MPCN) by ultrasonic chemical method [99]. Meanwhile, the U(VI) removal rate of 3% MPCN remained above 88.0% after the fifth usage, indicating its excellent chemical stability. The reduction product of U(VI) is $(UO_2)O_2{\cdot}2H_2O$, rather than the traditional UO_2. This sediment was formed through the reaction of UO_2 with H_2O_2 and may form a passivation layer on the catalyst surface. However, no significant decrease in activity was observed in the experiment. It was speculated that the interface between the sediment and the catalyst was weak, and the sediment could be removed through regeneration treatment. By mixing 1.0 mol/L $NaHCO_3$ and 0.2 mL 1.0 mol/L HNO_3 under stirring for 1 h, the U(IV) species deposited on the catalyst surface was effectively removed. After washing with water and methanol following vacuum drying, the as-obtained catalyst could be reused for subsequent experiments. Dai et al. decorated carbon dots onto porous g-C_3N_4 (CNCD) to enhance U(VI) photoreduction [100]. In the fifth cycling experiment, the removal rate of U(VI) by CNCD-2 decreased from 95.26% to 90.08% and it still maintained a high catalytic activity. The U(VI) species was reduced to U(IV) by photogenerated electrons (e^-) and free $^{\bullet}O_2^-$ radicals, and was then deposited on the surface of CNCD in the form of metatudite ($(UO_2)O_2{\cdot}2H_2O$). The TEM and XRD results confirmed the formation of uranium minerals, and these products are low-solubility solid phases, achieving the permanent fixation of uranium. The material was regenerated by washing with 0.1 M hydrochloric acid solution for 12 h, followed by centrifugation, water washing and vacuum drying. The FT-IR and XRD spectra of CNCD-2 after regeneration are basically consistent with those of the fresh sample, confirming that the regeneration process did not damage the material structure. Hong et al. successfully achieved the configuration of Fe-N_x embedded in g-C_3N_4 (FeN_x/g-C_3N_4) through a one-step pyrolysis strategy [101]. FeN_2/g-C_3N_4 maintained a 98% removal efficiency for U(VI) after six cycles of experiments. The FT-IR result indicated that the structure of the as-prepared FeN_2/g-C_3N_4 was not obviously changed, proving that the desired photocatalyst displayed an excellent cycling stability. The XPS analysis revealed that Fe atoms were mainly incorporated in the Fe-N_x coordination form as cationic forms (Fe^{2+}/Fe^{3+}) without metal Fe^0 forms. Moreover, no Fe leaching was detected by ICP-OES, indicating that the strong coordination between Fe and N inhibited the loss of metal active sites. Li et al. synthesized seven kinds of carbon dot/carbon nitride (CDs/CN) composites and screened out SerCDs/CN as having the best performance in photo-assisted uranium removal [102]. Moreover, Liu et al. and Xue et al. utilized a simple wet chemical method to couple g-C_3N_4 with carbon dots and poly-pyrrole (PPy) molecules, respectively, by forming CD-C_3N_4 and PPy/CN, of which both exhibited superior behavior for the removal and recovery of uranium from wastewater [103,104]. Dai et al. designed and synthetized a $ZnIn_2S_4$/g-C_3N_4 (ZISCN) heterojunction photocatalyst by in situ generation of $ZnIn_2S_4$ nanoparticles on g-C_3N_4, which efficiently extracted and converted soluble U(VI) ions into $(UO_2)O_2{\cdot}2H_2O$ solids, as depicted in Figure 7B [19]. After five consecutive cycles of photocatalytic uranium removal, the removal rate of U(VI) by ZISCN-2 remained above 85%, indicating that the material exhibited good stability and reusability. During photocatalytic reaction, rod-shaped uranium-containing products $(UO_2)O_2{\cdot}2H_2O$ were formed on the surface of ZISCN. Through XPS and EDX measurement, uranium-bearing products that existed in a hexavalent state were further confirmed. The catalytic activity was not reduced due to the formation of this deposition layer, possibly because the products were loosely attached to the surface and did not completely cover the active sites. Using 0.1 M HCl as the eluent, acid washing could effectively remove the uranium products deposited on the surface, achieving material regeneration. The

cycling experiments verified that superior activity and stability for ZISCN were achieved with simple operation and low cost. Furthermore, one-dimensional g-C_3N_4 nanorods were grown in situ on two-dimensional $ZnIn_2S_4$ nanosheets by Zheng et al. to construct a unique g-C_3N_4@$ZnIn_2S_4$ nanocomposite photocatalyst for efficient photocatalytic removal of U(VI) [105]. After five cycling tests, the removal efficiency of U(VI) over 7.5% CN@ZIS remained above 90%, and a slight decrease in efficiency was caused by inevitable mass loss of the catalyst during the cycling process. During reaction, the U(VI) species was reduced to the insoluble U(IV) and deposited on the catalyst surface, which might cover surface active sites. However, after the cycling experiment, the efficiency only decreased by approximately 7%, indicating that the passivation effect was relatively weak. Moreover, the leaching concentrations of Zn and in were extremely low, which was attributed to the strong interfacial interaction of the S-type heterojunction, thereby inhibiting the dissolution of metal ions. However, the S-scheme heterojunction remains in the concept verification stage, and the electron transfer path is highly sensitive to the OP/RP energy-level difference and interface dipole, with high requirements for reproducibility in preparation.

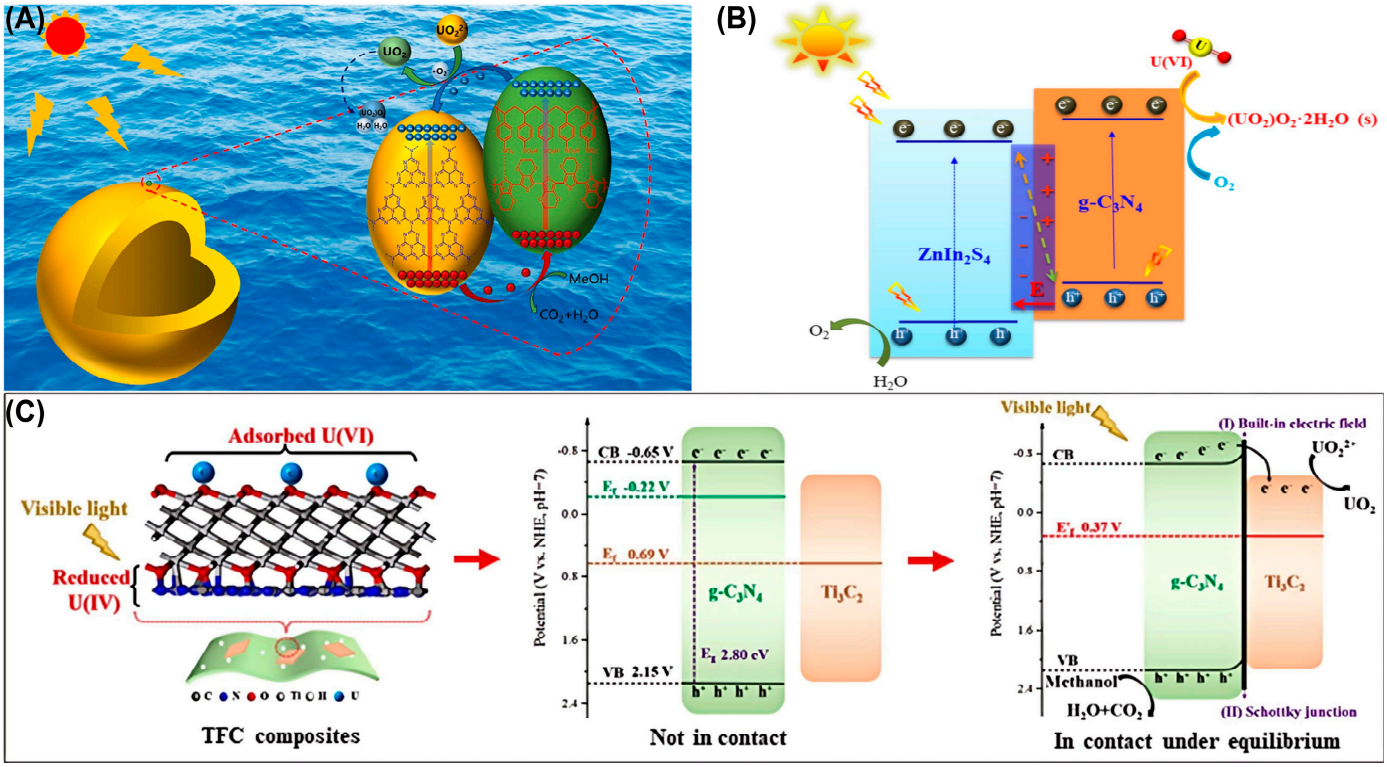


Figure 7. (**A**) Schematic diagram of the band structure for a hollow spherical PEDOT:PSS@HCN. Reprinted with permission from ref. [78]. (**B**) Possible mechanism of photocatalytic removal of U(VI) by ZISCN. Reprinted with permission from ref. [19]. (**C**) The photocatalytic mechanism of a TFC composite. Reprinted with permission from ref. [1].

Table 1. Summary of photocatalytic properties for g-C_3N_4-based heterojunctions.

Photocatalyst(s)	Type	Initial U(VI) Concentration	Catalyst Dose	Pre-Absorption Time	pH	Light Absorption	Optimal Extraction Efficiency	Optimal Rate Constants	Reference
$CdS/g\text{-}C_3N_4$	Type-II	23.8 mg/L	1.00 g/L	120 min	6.00	visible light	100% in 6 min	0.6410 min^{-1}	[70]
ipCN	Type-II	-	1.00 g/L	120 min	5.03	visible light	98% in 20 min	0.1540 min^{-1}	[68]
$SnS_2/g\text{-}C_3N_4$	Type-II	40.0 mg/L	0.80 g/L	-	5.00	visible-light to near-infrared region	92.74% in 90 min	0.02974 min^{-1}	[71]
FMCN	Type-II	40.0 mg/L	1.00 g/L	60 min	5.50	visible light	86.8% in 75 min	0.02695 min^{-1}	[69]
CNNS@CdS	Type-II	50.0 mg/L	0.30 g/L	60 min	5.00	visible light	95.7% in 120 min	-	[75]
$AgVO_3\text{-}InVO_4/g\text{-}C_3N_4$	Z-scheme	10.0 mg/L	0.10 g/L	30 min	7.00	visible light	98.7% in 20 min	0.1220 min^{-1}	[91]
$BiVO_4$/HCN	Z-scheme	40.0 mg/L	-	30 min	6.00	visible light	98.5% in 45 min	0.0997 min^{-1}	[95]
CN/Ni-MOF	Z-scheme	40.0 mg/L	0.48g/L	30 min	6.00	visible light	94.24% in 20 min	0.0877 min^{-1}	[97]
$MoS_2/g\text{-}C_3N_4$	Z-scheme	20.0 mg/L	0.91g/L	30 min	4.50	visible light	82% in 60 min	-	[87]
$g\text{-}C_3N_4/Ag/TiO_2$	Z-scheme	10.0 mg/L	0.40 g/L	30 min	5.00	visible light	99% in 30 min	-	[6]
MPCN	S-scheme	50.0 mg/L	1.00 g/L	120 min	5.00	visible light	99.75% in 60 min	0.1265 min^{-1}	[99]
$FeN_x/g\text{-}C_3N_4$	S-scheme	50.0 mg/L	0.50 g/L	60 min	6.00	visible light	99% in 60 min	0.091 min^{-1}	[101]
PPy/CN	S-scheme	40.0 mg/L	0.50 g/L	-	6.00	visible light	90% in 20 min	0.079 min^{-1}	[104]
$g\text{-}C_3N_4/LaFeO_3$	S-scheme	23.8 mg/L	0.20 g/L	120 min	5.00	visible light	93.8% in 40 min	-	[98]
CNCD	S-scheme	20.0 mg/L	0.17g/L	-	5.0 ± 0.02	visible light	95.26% in 50 min	-	[100]

Defect engineering offers another new integrated approach for the coupled adsorption–catalysis process of g-C_3N_4 in photocatalytic uranium extraction. Effective functionalization promotes the adsorption and activation of uranyl ions under mild conditions, optimizes the band position to ensure thermodynamic feasibility, and constructs electron traps to accelerate carrier separation, significantly improving uranium extraction efficiency. Defect engineering can increase the utilization rate of visible light, simultaneously enhance selectivity and capacity, and the process is simple and scalable. For instance, Li et al. constructed a C_3N_4-CeO_{2-x} heterojunction with abundant oxygen vacancies for the photoreduction of U(VI) in organic radioactive wastewater under visible light. Photoelectrons were transferred from g-C_3N_4 to CeO_{2-x} through the built-in electric field generated by the heterojunction and captured by shallow traps produced by surface vacancies, thus achieving spatial separation (Figure 8A,B) [20]. The U(VI) photoreduction rate constant of the CN-CeO_{2-x}heterojunction was 39 times higher than that of the pure g-C_3N_4, significantly outperforming existing g-C_3N_4-based materials. Through the synergistic effect of the heterostructure and oxygen vacancies, the separation efficiency of the photogenerated carriers was increased by approximately 125%, and the carrier lifetime was extended to 2.25 times that of pure g-C_3N_4 (τ_3 from 72.54 s to 163.14 s). This breakthrough occurred at the kinetic level, thus overcoming the charge recombination bottleneck of traditional photocatalysts. Dai et al. synthesized a K^+-doped and cyano-co-modified defective g-C_3N_4 (KHCN) photocatalyst via a simple one-step alkaline etching process [106]. The alkaline corrosion not only increased the specific surface area of KHCN, enhancing its adsorption of uranium, but also significantly accelerated the photocatalytic removal rate of uranium by introducing K^+ and cyano groups. Moreover, Hu et al. developed a novel hypoxic Co_3O_{4-x}/graphitic phase carbon nitride p-n heterojunction for the efficient photo-assisted extraction of uranium from seawater [5]. Discrete Fourier transform calculations indicated that the re-distribution of molecular charge density, relying on the defect-coupled heterojunction synergy effect, formed an internal electric field, significantly enhancing the carrier separation efficiency and accelerating the carrier migration rate. Chen et al. adopted a defect engineering strategy to combine boron nitride quantum dots (BNQDs) and nitrogen-doped carbon quantum dots (N-CQDs) onto the surface of g-C_3N_4 (NCN). They prepared N-CQDs-x/NCN/BNQDs-y through co-catalyst co-chemical modification and interface chemical bond synergy [107]. Nitrogen defects in g-C_3N_4 promote carrier separation, C-C interface bonding between N-CQDs and g-C_3N_4, hydrogen bonding between BNQDs and g-C_3N_4, and electron and hole transfer by co-catalysts (Figure 8C,D). Wang et al. successfully synthesized a $Ti_3C_2T_x/CN_v/MnO_x$ (CTM) photocatalyst by constructing a dual-vacancy of N anion and Ti cation to induce hybridization, and used it for the efficient photoreduction of U(VI) without a sacrificial agent [108]. The rate constant (k) for the U(VI) photoreduction of the CTM photocatalyst was 8.5, 4.9, and 2.4 times higher than that of pure g-C_3N_4, single-site CN_v, and double-site CT, respectively. The removal rate for U(VI) reached 96.1% within 90 min over CTM photocatalyst, significantly outperforming most of the photocatalysts reported in the literature. The introduction of dual vacancies can change the charge distribution on the surface of the photocatalyst, effectively overcoming the disadvantage of the poor capture ability of U(VI) and reducing the bandgap. Particularly, the strategy of the dual-vacancy-induced co-catalyst hybridization effect promotes the accelerated accumulation of electrons and holes on the corresponding co-catalysts, participating in redox reactions, and greatly enhances the spatial separation of charges. However, defect engineering is limited by the narrow defect concentration window, decreased structural stability, and potential weakening of redox ability. Precise characterization and controllable preparation of defects are also challenging.

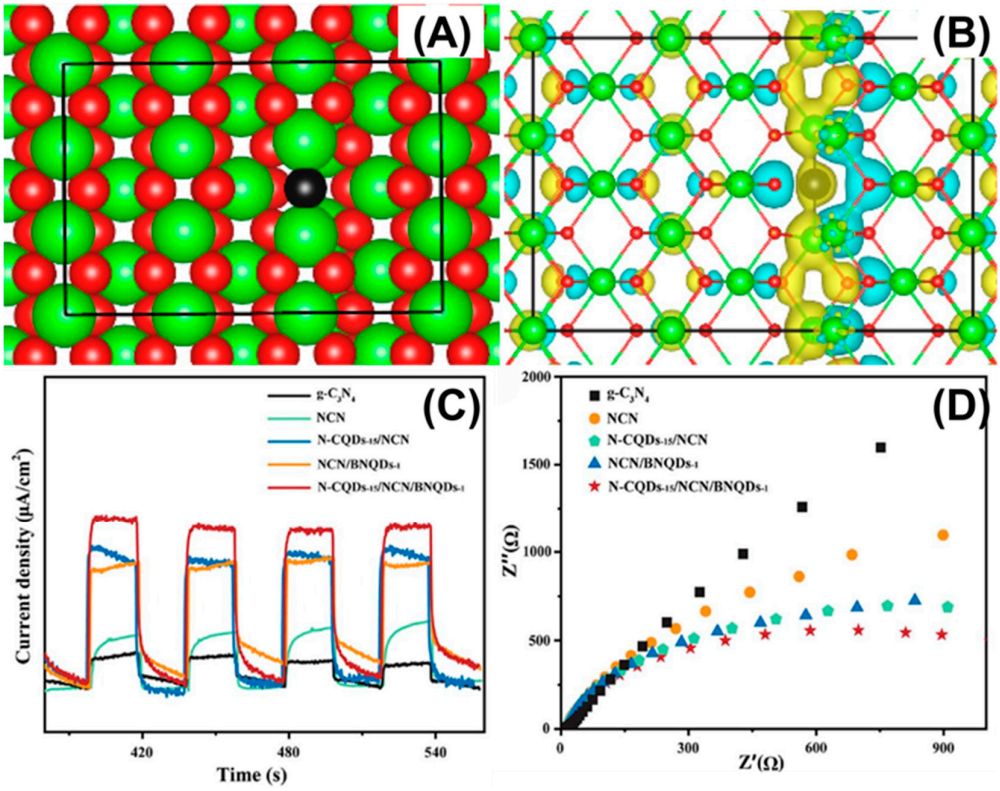


Figure 8. (**A**) Simulated structure of CeO_{2-X} (Ce and O atoms are shown in green and red, respectively, whereas the O atom near an oxygen vacancy is highlighted in black), and (**B**) charge energy difference of CeO_{2-X}. Reprinted with permission from ref. [20]. (**C**) Transient photocurrent response and (**D**) EIS Nyquist plots. Reprinted with permission from ref. [107].

The photocatalytic efficiency of g-C_3N_4 for uranium extraction can also be enhanced by introducing functional groups. Some functional groups can form a stable coordination with UO_2^{2+}, significantly improving the selective adsorption capacity for uranium. Moreover, functional groups act as "pre-concentration" sites, effectively enriching uranium ions before photocatalytic reduction, thereby enhancing the reaction efficiency. Additionally, functional groups can introduce defects or electronic states, adjusting the band structure and improving the efficiency of photogenerated electrons. Finally, certain functional groups can serve as electron traps, delaying the recombination process and increasing the photocatalytic efficiency. Gao et al. successfully synthesized a porous g-C_3N_4 nanosheet (DCNNS) photocatalyst co-modified with heteroatoms (Zn + C) and cyano groups [109]. The formation of cyano groups greatly broadened the light response range and, as a strong electron-withdrawing group, enhanced the separation rate of charge carriers. Similarly, Li et al. was dedicated to achieving the photoreduction of U(VI) in carbonate-containing systems by developing an efficient photocatalyst [3]. Carboxylated carbon nitride (CCN) catalysts (CCN-5 and CCN-24) with different carboxyl contents were prepared by the oxidating of bulk carbon nitride (BCN). The modification of electron-withdrawing carboxyl groups lowered the conduction band position and enhanced the separation efficiency of electrons and holes, which is beneficial for the photocatalytic reduction of U(VI) (Figure 9A). Zhou et al. combined amidoxime groups with carbon nitride to synthesize amidoxime-based carbon nitride (NCN-AO) with abundant nitrogen defects [11]. The uranium removal rate constant of NCN-AO in a 100 mg/L uranium solution was 0.0142 min^{-1}, which was significantly higher than that of ordinary carbon nitride (CN) at 0.0085 min^{-1}, indicating an approximately 67% improvement in its photocatalytic reduction efficiency. In 100 mg/L of uranium solution, the removal rate of uranium by NCN-AO was 99%, demonstrating

specific and selective adsorption for uranium (Figure 9B). Yu et al. successfully synthesized amidoxime-rich g-C_3N_4 (AO-C_3N_4) from the cyanide-rich precursor of uranium extraction from seawater by a simple amidoxime formation process under light assistance [15]. The amidoxime groups not only serve as efficient binding sites for U(VI) but also significantly enhance the visible-light absorption capacity and carrier separation efficiency of AO-C_3N_4 by introducing defect levels, endowing AO-C_3N_4 with excellent photocatalytic activity for light-assisted uranium extraction. Meanwhile, Hu et al. successfully prepared cyanide-functionalized g-C_3N_4 (g-C_3N_4-CN) with an isomeric structure for the adsorption and photoreduction of U(VI), achieving highly efficient photocatalytic extraction of uranium from seawater [110]. As a key component of the isomeric structure, cyanide not only significantly promotes the separation of photogenerated charges in g-C_3N_4-CN from the electrons enriched around it, but also greatly enhances the adsorption capacity and selectivity of g-C_3N_4-CN for U(VI) through complexation with U(VI). Inspired by this work, Li et al. prepared amidoxime-functionalized g-C_3N_4 (g-C_3N_4-ao) by grafting amidoxime groups onto g-C_3N_4, and utilized the lone pairs on O and N atoms as bidentate ligands for the complexation of uranium ions [111]. The desired g-C_3N_4-AO achieved the uranium adsorption equilibrium within 30 min, which was significantly faster than similar materials, indicating that chemical adsorption was the rate-determining step, and the introduction of the amine oxime group significantly enhanced the adsorption rate. In addition, Wang et al. reported a one-step calcination method to synthesize polymerized carbon nitride (SCN-C_3N_4), which combines cyano (-C≡N) modification and S-atom doping for highly efficient uranium extraction [112].

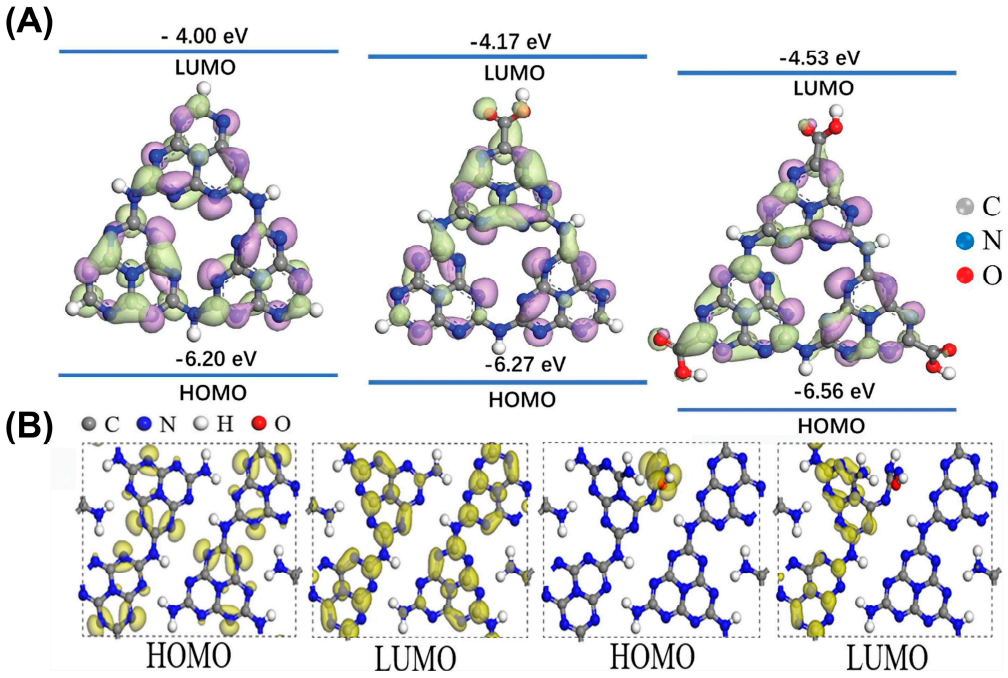


Figure 9. (**A**) Molecular orbital energies and structures of raw and carboxylated g-C_3N_4, HOMO: highest occupied molecular orbital, LUMO: lowest unoccupied molecular orbital. Reprinted with permission from ref. [3]. Copyright 2021, Elsevier. (**B**) HOMO and LUMO for CN and NCN-AO. Reprinted with permission from ref. [11].

4. Modularization Design and Application at the Industrial Level

After long-term recycling for uranium extraction from water bodies, g-C_3N_4-based catalysts suffer from surface passivation, structural oxidation, loss of active sites, agglomeration and delamination, etc. However, they still possess relatively high structural stability

under light and water corrosion. Through magnetic modification recovery strategies such as magnetic core loading, magnetic fiber fixation, and magnetic-light synergy, efficient recovery and recycling can be achieved without affecting their photocatalytic activity. Future research can focus on surface atomic-level regulation to enhance uranium selectivity, self-cleaning surface design to reduce deposition, and intelligent responsive magnetic carriers for closed-loop extraction.

At present, researchers have conducted extensive studies on powder g-C_3N_4, while its practical application is restricted by the prominent limitation of difficult separation. Magnetic strategies, three-dimensional carrier immobilization, and hydrogel membrane loading can help g-C_3N_4-based catalysts achieve large-scale industrial practical application. Magnetic composites, as the most common strategy, can achieve magnetic separation within 30 s while maintaining high recovery and cycling retention rates, which is suitable for industrialization. The thin film form of hydrogel membranes allows for direct removal without filtration and they can also be recycled multiple times. Three-dimensional carrier immobilization can enhance mechanical strength, prevent powder loss, and is suitable for continuous flow systems. After subsequent solid–liquid separation, uranium needs to be eluted with 0.1 M Na_2CO_3 or dilute HCl/HNO_3. The UO_{2+x} deposited on the catalyst surface is re-oxidized to UO_2^{2+} and enters the solution or forms $UO_2(CO_3)_3^{4-}$ complexes. Finally, NH_4OH or NaOH is added to adjust the pH to 4–6 to form U_3O_8 or UO_3 precipitates, achieving a closed process. At present, modular engineering has been studied in both g-C_3N_4-based adsorbents and g-C_3N_4-based catalysts. The performance of powdered materials can be affected at any time by gravity, vibration, and fluid erosion. Therefore, the designed three-dimensional foam and three-dimensional sponge materials can integrate the solid skeleton and continuous porous space into one, providing structural advantages that powders cannot achieve simultaneously. For instance, Zhu et al. reported a simple method for synthesizing a three-dimensional macroscopic g-C_3N_4 sponge from a melamine–formaldehyde (MFCN) resin through thermal polymerization [113]. This method makes extraction from an aqueous solution easy. A Schiff base reaction was designed to modify g-C_3N_4 sponge composites (MFCN-DETA, MFCN-TETA and MFCN-TEPA) with different organic amines (diethylenetriamine, triethylenetetramine and tetraethylenepentamine) (Figure 10A). Similarly, Momin et al. synthesized a cost-effective three-dimensional material by freeze-drying method in sodium alginate (SA) to encapsulate g-C_3N_4-layered double oxide (GCN-LDO), which was then used to extract uranium (U(VI)) from actual water bodies [114]. As shown in Figure 10B, a chemical interaction was formed between the sodium alginate-g-C_3N_4-layered double oxide (SA-GCN-LDO) sponge and the metal ions. In addition, Lingamdinne et al. investigated the removal of U(VI) from aqueous solutions using magnesium–iron-layered double hydroxide/g-C_3N_4 (LDH/g-C_3N_4) foam [115]. The metal ion adsorption process involves the coordination of covalent and electrostatic (non-covalent) interactions between metal ions and the surface of LDH/g-C_3N_4, which are enhanced by functional groups. Even after three regeneration cycles with EDTA, the foam maintained a considerable removal efficiency (75%), demonstrating excellent stability and reusability. Continuous fixed-bed column experiments further verified the practical feasibility of the material, achieving a long breakthrough time. With the increase in bed height, the adsorption capacity of the LDH/g-C_3N_4 foam increased, indicating that LDH/g-C_3N_4 foam has the potential for industrial application as an environmentally friendly U(VI) removal adsorbent. The purpose of subsequent research is to cut the three-dimensional sponge materials into uniform sizes, with each piece loading the same amount of g-C_3N_4, and achieve batch replacement in future. Unit standardization can be realized and then upgraded to modularization. Zhou et al. prepared a composite carbon aerogel (CNQDs/rGO) using CNQDs and graphene oxide as monomers through a simple one-step hydrothermal method [116]. ZIF-67 crystals

were directly deposited on the template (denoted as CNQDs/rGO/ZIF-67 carbon aerogel (CGZCA)) (Figure 10C). As for the photocatalyst, Qin et al. encapsulated the photocatalytic heterojunction of graphene oxide/g-C_3N_4 (GO/g-C_3N_4) through fiber spinning to obtain graphene oxide/g-C_3N_4/polyacrylonitrile oxime (GO/g-C_3N_4/PAO) films with adsorption and photoreduction capabilities for U(VI) [117]. The enhanced adsorption capacity of GO/g-C_3N_4/PAO nanofibers was achieved through the synergistic effect of amino oxime groups in PAO and the photocatalytic performance of GO/g-C_3N_4. Moreover, Yu et al. proposed a dual-regulation strategy to fabricate visible-light-responsive AO-CS/Cds porous few-layer g-C_3N_4 nanofiber membranes (SN-ACP) by electrospinning technology. SN-ACP possesses dual functions of adsorption and photocatalytic uranium extraction [118]. The ACP nanofiber membrane can address the drawbacks of SN nanoparticles, such as easy aggregation and difficulty in recovery, while SN nanoparticles can further enhance the uranium extraction capacity and selectivity of the ACP nanofiber membrane. Wu et al. firstly reported a novel C_3N_5/reduced graphene oxide (C_3N_5/RGO) aerogel photocatalyst with a three-dimensional macroscopic morphology, and further demonstrated that it was formed from a microscopic 2D/2D nanosheet Mott–Schottky heterojunction [2]. The macroscopic three-dimensional morphology of the C_3N_5/RGO aerogel effectively avoids the rate-measurement step in the uranium enrichment process and the secondary pollution of the environment by nanomaterials. Li et al. designed a photoactive hydrogel made of carboxyl-functionalized g-C_3N_4/CdS (CCN/CdS) for uranium extraction [4]. The hydrogel catalyst has excellent stability, good recyclability, outstanding anti-fouling activity and easy separability, all of which are required for uranium extraction from seawater.

Reactor and scale-up experiments are equally crucial for the practical industrial application of g-C_3N_4-based catalysts. In current research on scale-up experiments, light sources are mainly divided into artificial light sources such as LEDs and natural light. Natural light is suitable for outdoor or marine scenarios, while LED arrays are beneficial for the deep purification of industrial wastewater. In terms of spectral matching, g-C_3N_4 has the strongest absorption in the 420–470 nm blue–violet light range. Natural light only accounts for 15% of visible light in this band. Under the same power density, the photon utilization rate of LEDs can be customized to over 40%. Moreover, the intensity of natural light varies greatly, which is not conducive to maintaining the optimal reaction rate constant. Additionally, the infrared part of natural light causes the system to heat up, which, while suppressing oxygen quenching, easily leads to thermal deactivation of the catalyst. LED arrays with heat sinks can effectively control the temperature. In terms of phase systems, heterogeneous systems have advantages such as easy separation, high selectivity, and low operating costs, and have been verified for scalability at pilot scale. Homogeneous systems only have advantages in extremely low concentrations or at the research stage of mechanisms, and their industrial prospects are limited. Regarding the initial uranium concentration, low concentrations at the ppb level are generally found in seawater, while high concentrations at the ppm level are mainly in mine wastewater and industrial high-level radioactive waste liquids. For low concentrations at the ppb level, strategies such as extended residence time and selective adsorption are generally adopted, which have high unit energy consumption but are feasible in terms of overall value due to the high value of uranium in seawater. For high concentrations at the ppm level, strategies such as rapid reduction–crystallization–magnetic separation are usually employed, which have low energy consumptions and can simultaneously recover valuable associated metals to maximize profits. The scale-up experiments of catalytic uranium extraction have three mature routes: modular, zero grid electricity, and zero chemical reagents, maintaining over 80% efficiency in photoelectric synergy under night or weak light conditions, zero sludge discharge through membrane catalytic coupling without magnetic powder, and “zero grid

electricity" operation in offshore or remote mining areas through photovoltaic direct drive. The combination of in situ leaching with low processing costs and low environmental risks can achieve the industrial goal of extracting 1000 tons of uranium per year from seawater and zero discharge of mine wastewater within the next three years.

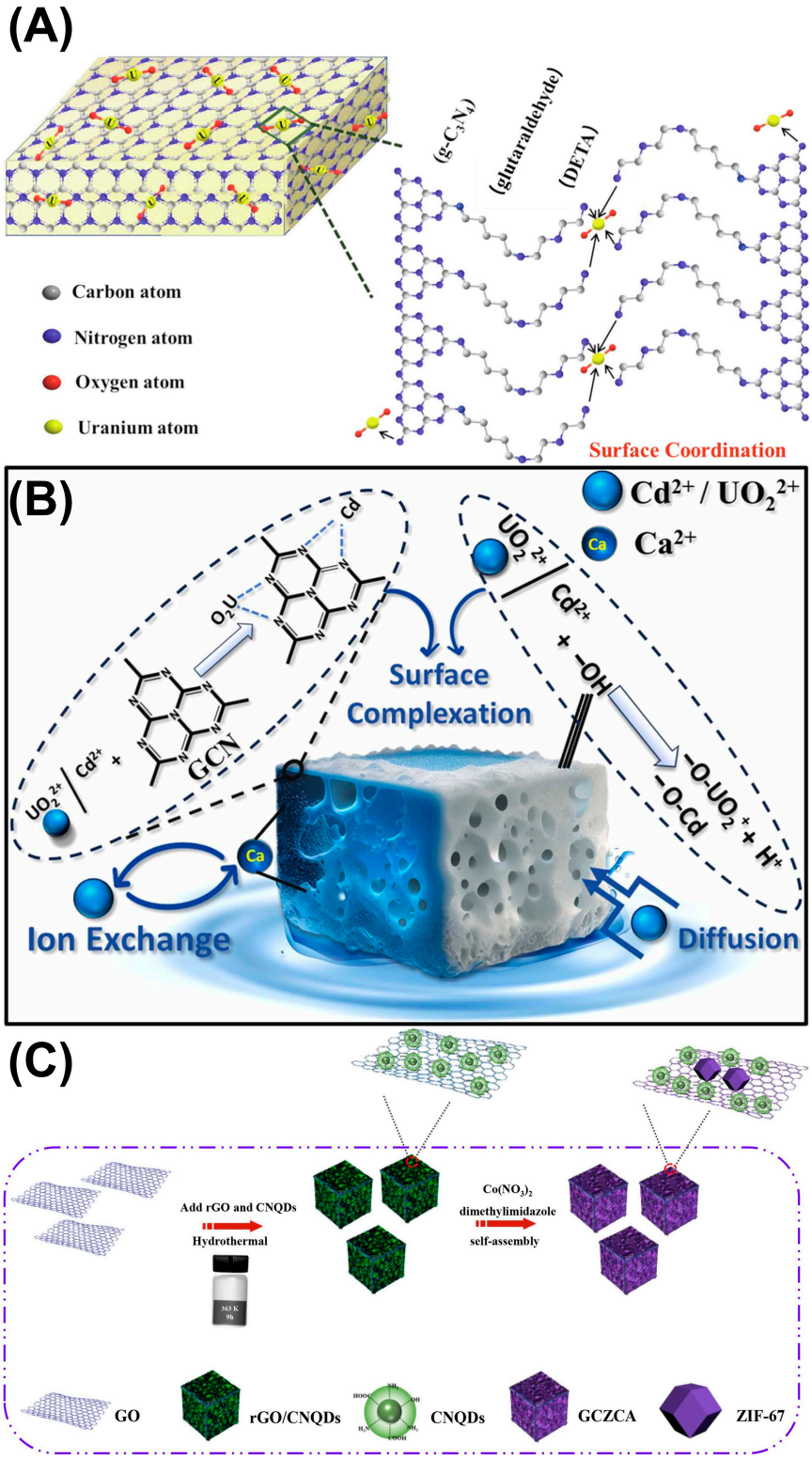


Figure 10. (**A**) Proposed mechanisms for the adsorption of U(VI) onto the MFCN-DETA. Reprinted with permission from ref. [113]. (**B**) Schematic synergistic adsorption mechanism of U(VI) and Cd(II)

on SA-GCN-LDO sponge. Reprinted with permission from ref. [114]. (**C**) The GCZCA preparation flow chart. Reprinted with permission from ref. [116].

For reactor design, batch processing reactors are either static or have low-speed stirring, which causes catalysts to easily settle, the light path to shorten over time, and UO_2 particles to gradually cover active sites, necessitating regular acid washing. In the later stage of the reaction, the concentration is low, the driving force weakens, and the rate constant decreases. Batch reactors can be combined with magnetic separation to handle low-flow, high-concentration wastewater, with the advantage of being the most economical. Continuous-flow reactors use laminar or turbulent forced circulation, and sedimentation is carried away by fluid shear, allowing for self-cleaning of the catalyst surface and maintaining a high circulation retention rate. By supplementing light or catalysts between stages, a high driving force can be maintained, and the overall k value is relatively stable. Continuous-flow–rotating-disk or falling-film reactors can be linearly scaled up with stable efficiency, suitable for high-flow, low-concentration seawater. For high-concentration, high-value non-ferrous metals, microchannel continuous flow can achieve second-level residence time, with an investment payback period of less than one year. Nowadays, photocatalytic or electrocatalytic uranium extraction has completed the "laboratory–pilot–demonstration" three-level leap, with high scalability. In terms of economic cost, the comprehensive cost-per-ton of uranium has approached traditional processes, and it has better environmental compliance. It has the potential for ten-thousand-ton-level industrialization in the next 3–5 years.

5. Outlook and Challenges

At present, g-C_3N_4-based catalysts usually face problems such as insufficient active sites, recombination of photogenerated charges and holes, and as well the re-oxidation of U(IV), which majorly restrict the practical application of photocatalytic seawater uranium extraction. Under aerobic conditions, the re-dissolution of uranium-containing solids inevitably reduces the overall removal rate, and the re-oxidized U(IV) products may deposit on the catalyst surface, which causes catalyst poisoning by blocking active sites or destroying catalyst structure, thereby affecting the efficiency of photogenerated charge separation. To effectively realize the practical application of seawater uranium extraction, the recombination of photogenerated charges and holes under actual sunlight is an essential factor that must be taken into consideration. The recombination of photogenerated charge carriers reduces the utilization rate of photons and inhibits the oxidation half-reaction. During reactions, other electron acceptors can also compete for electrons with U(VI) to yield reactive oxygen species, thereby reducing the reduction selectivity. Therefore, the design and construction of g-C_3N_4-based catalysts should be optimized for adjusting the electric energy level, improving visible-light utilization, and inhibiting the recombination of photogenerated charges and holes, thereby contributing to achieving the practical application of photocatalytic uranium extraction from seawater on a large scale and in industrial applications.

Since the breakthrough from trial-and-error to intelligent prediction in catalyst design and screening with the aid of the elimination of the low-temperature reaction efficiency bottleneck by photothermal synergistic catalysis, and the integration of advanced technologies such as the bio-photocatalytic coupling system, which is the ultimate direction for green and low-carbon production, into the field of uranium reduction and enrichment based on g-C_3N_4 materials, interdisciplinary integration has ushered in a paradigm revolution from materials to systems, moving from the "material trial-and-error" direction to the new stage of "intelligent design–environmental adaptability–green and low-carbon", with the ultimate goal of building a solar-driven self-evolving purification system. Usually,

g-C_3N_4-based materials are positioned as a "front-end green reduction technology" rather than the "ultimate disposal technology", and they have industrialization potential. If these materials are to be promoted to the market, they should first target low- to medium-level uranium-containing wastewater, and it is not advisable to directly challenge high-level radioactive liquid waste at this stage. Driven by the triple forces of "dual-carbon" subsidies, CCER benefits, and the demand for nuclear safety governance, the best window for commercialization is presented.

Due to the complexity of the water bodies, it is necessary to improve the functional design to improve the reusability, anti-biofouling ability and stability of g-C_3N_4-based materials and promote the application of g-C_3N_4-based materials at the industrial level. Moreover, interdisciplinary research combined with photocatalysis and electrochemistry can explore new strategies. In a word, it is a multidisciplinary and comprehensive field, which needs abundant fundamental research and advanced techniques for characterization based on the chemical and physical properties of g-C_3N_4-based materials before the blueprint can be realized. With the development of nuclear energy, the reduction and enrichment of U(VI) from water bodies via photocatalysis is one of the most promising strategies to solve the energy crisis.

Author Contributions: Z.Z., X.Y. and S.P. conducted the information search and wrote the first draft of the review manuscript, and S.Z. revised the entire manuscript. All authors have read and agreed to the published version of the manuscript.

Funding: This research was supported by the Jing-Jin-Ji Regional Integrated Environmental Improvement National Science and Technology Major Project (2025ZD1203000), and the National Natural Science Foundation of China (grant numbers 22106047, 42507037, and 52200091).

Data Availability Statement: No new data were created or analyzed in this study. Data sharing is not applicable to this article.

Conflicts of Interest: The authors declare no conflicts of interest.

References

1. Yu, J.Q.; Zhang, H.S.; Liu, Q.; Yu, J.; Zhu, J.H.; Li, Y.; Li, R.M.; Wang, J. 2D/2D heterojunction of Ti_3C_2/porous few-layer g-C_3N_4 nanosheets for high-efficiency extraction of uranium (VI). *Sep. Purif. Technol.* **2023**, *312*, 123442. [CrossRef]
2. Wu, L.Z.; Yang, X.Y.; Chen, T.; Li, Y.; Meng, Q.; Zhu, L.; Zhu, W.K.; He, R.; Duan, T. Three-dimensional C_3N_5/RGO aerogels with enhanced visible-light response and electron-hole separation efficiency for photocatalytic uranium reduction. *Chem. Eng. J.* **2022**, *427*, 131773. [CrossRef]
3. Li, P.; Wang, Y.; Wang, J.J.; Dong, L.; Zhang, W.T.; Lu, Z.H.; Liang, J.J.; Pan, D.Q.; Pan, Q.H. Carboxyl groups on g-C_3N_4 for boosting the photocatalytic U(VI) reduction in the presence of carbonates. *Chem. Eng. J.* **2021**, *414*, 128810. [CrossRef]
4. Li, P.; He, T.; Wang, J.J.; Ou, N.Y.; Liang, J.J.; Wang, G.; Fan, Q.H. Realizing Direct Uranium Extraction from Seawater Using a Carboxyl-g-C_3N_4/CdS Hydrogel. *Small* **2024**, *20*, 2404417. [CrossRef]
5. Hu, E.M.; Liu, Q.; Qian, Z.S.; Zhong, Q.; He, J.H.; Xu, S.C.; Lu, T.M.; Li, J.; Chen, T.; Zhu, W.K. Unveiling Mechanistic Insight into Accelerating Oxygen Molecule Activation by Oxygen Defects in Co_3O_{4-x}/g-C_3N_4 p–n Heterojunction for Efficient Photo-Assisted Uranium Extraction from Seawater. *Small* **2024**, *20*, 2403105. [CrossRef]
6. Liu, Y.L.; Yuan, Y.L.; Ni, S.Y.; Liu, J.; Xie, S.B.; Liu, Y.J. Construction of g-C_3N_4/ag/TiO_2 Z-scheme photocatalyst and its improved photocatalytic U(VI) reduction application in water. *Water Sci. Technol.* **2022**, *85*, 2639–2651. [CrossRef]
7. Li, Y.; Huang, T.; Liu, X.L.; Chen, Z.S.; Yang, H.; Wang, X.K. Sorption-catalytic reduction/extraction of hexavalent Cr(VI) and U(VI) by porous frameworks materials. *Sep. Purif. Technol.* **2023**, *314*, 123615. [CrossRef]
8. Zhang, W.Z.; Li, L.; Gao, Y.H.; Zhang, D. Graphitic carbon nitride-based materials for photocatalytic reduction of U(VI). *New. J. Chem.* **2020**, *44*, 19961–19976. [CrossRef]
9. Lu, C.H.; Chen, R.Y.; Wu, X.; Fan, M.F.; Liu, Y.H.; Le, Z.G.; Jiang, S.J.; Song, S.Q. Boron doped g-C_3N_4 with enhanced photocatalytic UO_2^{2+} reduction performance. *Appl. Surf. Sci.* **2016**, *360*, 1016–1022. [CrossRef]
10. Meng, Q.; Yang, X.Y.; Wu, L.Z.; Chen, T.; Li, Y.; He, R.; Zhu, W.K.; Zhu, L.; Duan, T. Metal-free 2D/2D C_3N_5/GO nanosheets with customized energy-level structure for radioactive nuclear wastewater treatment. *J. Hazard. Mater.* **2022**, *422*, 126912. [CrossRef]

11. Zhou, Z.; Liu, Q.; Zhu, J.H.; Liu, J.Y.; Zhang, H.S.; Yu, J.; Chen, R.R.; Li, Y.; Wang, J.J. Defective carbon nitride ultrathin nanosheets enriched with amidoxime groups for enhanced visible light-driven reduction of hexavalent uranium. *Colloid Interf. Sci.* **2022**, *628*, 840–848. [CrossRef] [PubMed]
12. Wei, B.Q.; Luo, J.Y.; Lin, S.Y.; Li, Z.F.; Zhu, X.; Dong, Z.M.; Xiao, S.T.; Cao, X.H.; Liu, Y.H.; Zhang, Z.B. Exciton dissociation and electron transfer behavior of a novel Donor-Acceptor g-C_3N_4 organic semiconductor photocatalytic separation of uranium. *Sep. Purif. Technol.* **2023**, *318*, 123918. [CrossRef]
13. Wang, Z.R.; Li, W.H.; Wu, L.Z.; Wang, Z.; Gao, Y.L.; Cheng, L.K.; Chen, G.Y.; Zhao, Q.; Jiang, M.; Chen, Z.G.; et al. Nitrogen-rich carbon nitrogen polymers for enhancing the sorption of uranyl. *Chin. Chem. Lett.* **2022**, *33*, 3468–3473. [CrossRef]
14. Liu, C.L.; Guo, Y.D.; Li, S.H.; Xuan, K.; Guo, Y.P.; Li, J.; Wang, X.G.; Li, X.M.; Zhou, Z.K. Mesoporous sulfur-doped g-C_3N_4@attapulgite composite as an advanced photocatalyst for efficiently uranium(VI) recovery from aqueous solutions. *J. Environ. Chem. Eng.* **2024**, *12*, 112886. [CrossRef]
15. Yu, K.F.; Li, Y.; Cao, X.; Wang, R.X.; Zhou, L.; Wu, L.Z.; He, N.N.; Lei, J.; Fu, D.J.; Chen, T.; et al. In-situ constructing amidoxime groups on metal-free g-C_3N_4 to enhance chemisorption, light absorption, and carrier separation for efficient photo-assisted uranium(VI) extraction. *J. Hazard. Mater.* **2023**, *460*, 132356. [CrossRef]
16. Li, S.Y.; Niu, Z.W.; Pan, D.Q.; Cui, Z.P.; Shang, H.W.; Lian, J.; Wu, W.S. Efficient photoreduction strategy for uranium immobilization based on graphite carbon nitride/activated carbon nanocomposites. *Chin. Chem. Lett.* **2022**, *33*, 3581–3584. [CrossRef]
17. Wang, J.J.; Wang, Y.; Wang, W.; Ding, Z.; Geng, R.Y.; Li, P.; Pan, D.Q.; Liang, J.J.; Qin, H.B.; Fan, Q.H. Tunable mesoporous g-C_3N_4 nanosheets as a metal-free catalyst for enhanced visible-light-driven photocatalytic reduction of U(VI). *Chem. Eng. J.* **2020**, *383*, 123193. [CrossRef]
18. Zhang, G.Z.; Lei, T.; Wang, D.D.; Tian, X.D.; Wang, Y.; Yang, W.T.; Xu, Q.; Su, Z.M. One-step synthesis of O, P co-doped g-C_3N_4 under air for photocatalytic reduction of uranium. *J. Solid. State. Chem.* **2024**, *339*, 124941. [CrossRef]
19. Dai, Z.R.; Liang, B.C.; Chen, L.J.; Zhang, W.L.; Gao, Y.; Li, L. Rational construction of S-scheme $ZnIn_2S_4$/g-C_3N_4 heterojunction for effective sacrificial agent-free uranium photocatalysis in air. *Sep. Purif. Technol.* **2025**, *354*, 129241. [CrossRef]
20. Li, S.Y.; Pan, D.Q.; Cui, Z.P.; Xu, Y.; Shang, H.W.; Hua, W.W. Synergistic effects of oxygen vacancies and heterostructures for visible-light-driven photoreduction of uranium. *Sep. Purif. Technol.* **2022**, *301*, 121966. [CrossRef]
21. Yang, Z.Y.; Qi, C.H.; Yuan, P.L.; Hu, R.; Du, X.; Cheng, M. High-efficiency selective removal of U(VI) by phosphate-functionalized graphitic carbon nitride activated using guanidine phosphate. *J. Environ. Chem. Eng.* **2023**, *11*, 110272. [CrossRef]
22. Ding, L.; Chen, B.W.; Wang, Y.; Zhang, Y. High efficiency adsorption of uranium in solution using nano-TiO_2 loaded with g-C_3N_4. *Process Saf. Environ. Prot.* **2022**, *168*, 1049–1057. [CrossRef]
23. Wang, H.H.; Mei, P.; Huang, X.S.; Xiao, J.T.; Sun, Y.B. Uranyl(VI) boosting 3D g-C_3N_4 photocatalytic H_2O_2 production for U(VI) immobilization. *J. Clean. Prod.* **2022**, *330*, 129821. [CrossRef]
24. Dhanasekaran, A.; Perumal, I. Adsorption of aqueous uranium(VI) species on graphitic carbon nitride adsorbent (g-CNA): Kinetic, isotherm and thermodynamic studies. *J. Radioanal. Nucl. Chem.* **2024**, *334*, 79–91. [CrossRef]
25. He, Y.N.; Li, J.J.; Cheng, J.; Cherkasova, T.G.; Li, L. Phosphorous-modified porous graphitic carbon nitride activated by phytic acid for efficient, selective extraction and photoreduction of uranium from aqueous solutions. *New J. Chem.* **2025**, *49*, 5505–5512. [CrossRef]
26. Dhanasekaran, A.; Priyadarshini, N.; Perumal, I.; Suresh, G.; Sagadevan, S. Hydroxyapatite derived from eggshell embedded on functionalized g-C_3N_4 for synergistic extraction of U(VI) from aqueous solution. *Chemosphere* **2024**, *364*, 143018. [CrossRef]
27. Hu, B.W.; Wang, H.F.; Liu, R.R.; Qiu, M.Q. Highly efficient U(VI) capture by amidoxime/carbon nitride composites: Evidence of EXAFS and modeling. *Chemosphere* **2021**, *274*, 129743. [CrossRef] [PubMed]
28. Zhang, C.L.; Liu, Y.; Li, X.; Chen, H.X.; Wen, T.; Jiang, Z.H.; Ai, Y.J.; Sun, Y.B.; Hayat, T.; Wang, X.K. Highly uranium elimination by crab shells-derived porous graphitic carbon nitride: Batch, EXAFS and theoretical calculations. *Chem. Eng. J.* **2018**, *346*, 406–415. [CrossRef]
29. Chen, T.; Liu, T.; Zhou, L.; Li, M.X.; Meng, Q.; Yu, K.F.; Lian, J.; Zhu, W.K. Ternary boron carbon nitrides hollow nanotubes with tunable p-n homojunction for photo-assisted uranium extraction: A combined batch, EXAFS and DFT calculations. *Appl. Catal. B-Environ. Energy* **2022**, *318*, 121815. [CrossRef]
30. Zhang, X.Y.; Du, Y.; Deng, L.P.; Zhang, Z.Y.; Chen, Z.Q.; Dong, H.L. One-pot fabrication of nanoscale zero-valent iron scaffolded onto graphitic carbon nitride as bifunctional nanohybrid in sequestering U(VI) and Cr(VI) with boost performance and intrinsic mechanism. *Appl. Surf. Sci.* **2024**, *654*, 159437. [CrossRef]
31. Liang, L.P.; Xi, F.F.; Zhou, M.F.; Hu, B.W. Efficient U(VI) removal from aerobic solution by synergistic interaction of nano zero-valent iron with g-C_3N_4 and assessment of toxicity to microorganism. *J. Water Process Eng.* **2024**, *64*, 105630. [CrossRef]
32. Fu, H.; Pan, Y.H.; Cai, Z.Y.; Deng, Y.X.; Hou, M.C.; Wei, Y.Z.; Fujita, T.; Ning, S.Y.; Wang, Y.B.; Zhang, S.L.; et al. Bi_2O_3/g-C_3N_4 hollow core–shell Z-scheme heterojunction for photocatalytic uranium extraction. *Nano Res.* **2024**, *17*, 5845–5855. [CrossRef]

33. Zhang, Y.; Chen, Q.X.; Xiao, Q.X.; Shi, L.; Zhao, Z.; Wang, H.Q. Enhancement of CdS resistance to photocorrosion and photocatalytic removal of uranyl by complexation with N-deficient g-C_3N_4 under aerobic conditions. *Chemosphere* **2023**, *335*, 139022. [CrossRef] [PubMed]
34. Zhang, Y.K.; Deng, R.J.; Zeng, J.B.; Shi, F.Y.; Yang, S.Q.; Wu, Y.S.; Duan, T. Phosphorus functionalized carbon nitride for rapid adsorption of uranium from aqueous solution. *J. Radioanal. Nucl. Chem.* **2025**, *334*, 2227–2236. [CrossRef]
35. Dhanu, M.; Priyadarshini, N.; Perumal, I.; Suresh, G.; Santhamoorthy, M. Enhanced removal of uranium from aqueous solutions using 'oxygen donor' enriched graphitic carbon nitride adsorbent. *J. Radioanal. Nucl. Chem.* **2025**, *334*, 3535–3548. [CrossRef]
36. Wang, M.J.; Sun, W.X.; Li, M.; Wu, X.Y.; Chen, C.M.; Cai, T.; Zeng, Q.Y.; Hua, Y.L.; Wang, L.L.; Xie, H.J. π-electron injection activated dormant ligands in graphitic carbon nitride for efficient and stable uranium extraction. *J. Hazard. Mater.* **2024**, *478*, 135445. [CrossRef]
37. Ge, Y.J.; He, Z.Q.; Wu, J.; Wang, G.H.; Xie, S.B.; Liu, J.X. Manganese ferrite/porous graphite carbon nitride composites for U(VI) adsorption from aqueous solutions. *J. Radioanal. Nucl. Chem.* **2020**, *326*, 157–171. [CrossRef]
38. Wu, J.; Zheng, Z.H.; Zhu, K.H.; Xiang, C.; Wang, J.S.; Liu, J.X. Adsorption performance and mechanism of g-C_3N_4/UiO-66 composite for U(VI) from aqueous solution. *J. Radioanal. Nucl. Chem.* **2022**, *331*, 469–481. [CrossRef]
39. Xu, L.X.; Li, L.; Fang, P.; Chang, K.K.; Chen, C.G.; Liao, Q. Removal of uranium (VI) ions from aqueous solution by graphitic carbon nitride stabilized FeS nanoparticles. *J. Mol. Liq.* **2022**, *345*, 117050. [CrossRef]
40. Momin, Z.H.; Lingamdinne, L.P.; Kulkarni, R.; Pal, C.A.K.; Choi, Y.L.; Koduru, J.R.; Chang, Y.Y. Improving U(VI) retention efficiency and cycling stability of GCN-supported calcined-LDH composite: Mechanism insight and real water system applications. *Chemosphere* **2024**, *346*, 140551. [CrossRef]
41. Zhao, G.D.; Xiao, H.R.; Tang, X.L.; Liu, Q. Adsorption performance of prussian blue supported graphitic carbon nitride composite (prussian blue/g-C_3N_4) for the removal of U(VI) from aqueous solutions. *J. Radioanal. Nucl. Chem.* **2024**, *333*, 5173–5182. [CrossRef]
42. Fang, W.X.; Sun, C.; Chang, Z.Y.; Wang, Y.D.; Wang, X.X.; Yu, S.J. Uranium removal by magnetic $ZnFe_2O_4$@g-C_3N_4 nanocomposites: Characterization and mechanism. *Appl. Surf. Sci.* **2025**, *771*, 164068. [CrossRef]
43. Li, Z.Q.; Xie, Z.B.; Wang, B.; Gong, J.Y.; Xue, J.M.; Le, Z.G. Gas-sculpted g-C_3N_4 for efficient photocatalytic reduction of U(VI). *J. Radioanal. Nucl. Chem.* **2020**, *326*, 1805–1817. [CrossRef]
44. Liu, S.; Wang, Z.; Lu, Y.X.; Li, H.P.; Chen, X.J.; Wei, G.Y.; Wu, T.; Maguire, D.J.; Ye, G.; Chen, J. Sunlight-induced uranium extraction with triazine-based carbon nitride as both photocatalyst and adsorbent. *Appl. Catal. B-Environ. Energy* **2021**, *282*, 119523. [CrossRef]
45. Alberto, S.A.; Eva, S.H.; Natalia, L.L.; Vicente, G.G.; José, C.G.; Jesús, M.G.; Pablo, M.R. Multifunctional nanocarriers based on chitosan oligomers and graphitic carbon nitride assembly. *Materials* **2022**, *15*, 8981. [CrossRef]
46. Li, Z.F.; Zhang, Z.B.; Zhu, X.; Meng, C.; Dong, Z.M.; Xiao, S.T.; Wang, Y.C.; Wang, Y.Q.; Cao, X.H.; Liu, Y.H. Exciton dissociation and transfer behavior and surface reaction mechanism in donor–acceptor organic semiconductor photocatalytic separation of uranium. *Appl. Catal. B-Environ. Energy* **2023**, *332*, 122751. [CrossRef]
47. Liu, S.; Li, X.D.; Huang, L.Q.; Qing, Q.; Maguire, D.J.; Chae, N.; Wang, Z.; Chen, J.; Lu, Y.X. Molten salt synthesis of carbon nitride nanostructures at different temperatures for extracting uranium from seawater. *ACS Appl. Nano Mater.* **2023**, *6*, 4782–4792. [CrossRef]
48. Wu, Z.W.; Wang, B.; Zhu, Y.A.; Xue, J.M.; Nie, Y.D.; Xie, Z.B.; Le, Z.G. Synthesis of crystalline carbon nitride with molten salt thermal treatment for efficient photocatalytic reduction and removal of U(VI). *Res. Chem. Intermed.* **2023**, *49*, 1801–1817. [CrossRef]
49. Dang, Z.H.; Gao, W.J.; Chu, Y.Y.; Pang, B.P.; Zhang, L. Nitrogen-rich carbon nitride with heptazine phase controlled by pyrolysis temperature towards photocatalytic U(VI) reduction. *Chem. Phys.* **2024**, *587*, 112421. [CrossRef]
50. Liu, Z.M.; Li, Y.Y.; Yao, S.Q.; Zhou, R.C.; Lin, G.T.; Fu, Y.Z.; Zhou, Q.X.; Wang, W.; Chi, W.J. Rich electron delocalization structure in carbon nitride inducing radical transfer for high-performance photocatalytic uranyl reduction. *Carbon Energy* **2024**, *6*, e636. [CrossRef]
51. Song, Z.K.; Yan, C.P.; Qiu, J.L.; Liu, C.; Zhu, Y.A.; Wang, B.; Xie, Z.B.; Chen, G.; Li, K.Q.; Le, Z.G. Photocatalytic reduction of the uranium (VI) by ultra-thin porous g-C_3N_4 nanosheets synthesized via microwave-assisted. *J. Environ. Chem. Eng.* **2024**, *12*, 113951. [CrossRef]
52. Wu, Z.W.; Xie, Z.B.; Zhu, Y.A.; Wang, B.; Nie, Y.D.; Qiu, J.L.; Le, Z.G. Solvent-regulated self-assembled carbon nitride for photocatalytic reduction of U(VI) in water. *Photochem. Photobiol. Sci.* **2024**, *23*, 651–664. [CrossRef]
53. Zhang, W.L.; Chen, L.J.; Yang, S.C.; Chen, Z.J.; Dai, Z.R.; Li, L. Design and synthesis of graphitic carbon nitride photonic crystals for efficient photocatalytic removal of U(VI). *J. Environ. Chem. Eng.* **2024**, *12*, 114854. [CrossRef]
54. Li, Y.H.; Shi, L.; Mao, Y.; Wang, H.Q. Efficient reduction of uranyl under aerobic conditions by sodium and potassium co-doped carbon nitride. *Chem. Eng. J.* **2022**, *446*, 136872. [CrossRef]
55. Nie, Y.D.; Zhu, Y.A.; Lu, X.Y.; Qiu, J.L.; Wang, B.; Xie, Z.B. Cu doped crystalline carbon nitride with increased carrier migration efficiency for uranyl photoreduction. *Chem. Eng. J.* **2023**, *477*, 146908. [CrossRef]

56. Liu, S.; Zhao, N.; Zheng, L.Y.; Fosyer, R.I.; Yang, W.; Wang, Z.; Liu, Y.X. Enhanced visible light photocatalytic activity of pt cluster modified carbon nitrides for U(VI) removal. *J. Environ. Chem. Eng.* **2024**, *12*, 114211. [CrossRef]
57. Wei, W.; Luo, L.Q.; Liu, S.J.; Zhou, Y.M.; Ma, J.G. Enhancing the photocatalytic performance of g-C_3N_4 by using iron single-atom doping for the reduction of U(VI) in aqueous solutions. *J. Solid State Chem.* **2022**, *312*, 123160. [CrossRef]
58. Hu, Z.F.; Liu, Z.X.; Tay, C.C.; Bao, L.F.; Qiu, M.Q. Investigating the photocatalytic reduction of U(VI) over a single-atom Fe complex catalyst. *J. Mol. Liq.* **2024**, *411*, 125774. [CrossRef]
59. Lu, C.H.; Zhang, P.Z.; Jiang, S.J.; Wu, X.; Song, S.Q.; Zhu, M.S.; Luo, Z.Z.; Li, Z.; Liu, F.; Liu, Y.H.; et al. Photocatalytic reduction elimination of UO_2^{2+} pollutant under visible light with metal-free sulfur doped g-C_3N_4 photocatalyst. *Appl. Catal. B-Environ. Energy* **2017**, *200*, 378–385. [CrossRef]
60. Dang, Z.H.; Ding, L.; Zhao, X.; Zhang, L.; Zhang, S. Sulfur doped N-rich nitrogen carbon nanocatalysts for enhancing photocatalytic reduction of uranium(VI). *J. Radioanal. Nucl. Chem.* **2024**, *333*, 4107–4118. [CrossRef]
61. Gong, J.Y.; Xie, Z.B.; Wang, B.; Li, Z.Q.; Zhu, Y.A.; Xue, J.M.; Le, Z.G. Fabrication of g-C_3N_4-based conjugated copolymers for efficient photocatalytic reduction of U(VI). *J. Environ. Chem. Eng.* **2021**, *9*, 104638. [CrossRef]
62. Xue, J.M.; Wang, B.; Li, Z.Q.; Xie, Z.B.; Le, Z.G. Bromine doped g-C_3N_4 with enhanced photocatalytic reduction in U(VI). *Res. Chem. Intermed.* **2022**, *48*, 49–65. [CrossRef]
63. Liu, Y.L.; Gao, Y.; Chen, L.J.; Li, L.; Ding, D.X.; Dai, Z.R. MnOx-decorated oxygen-doped g-C_3N_4 with enhanced photocatalytic activity for efficient removal of uranium(VI). *Sep. Purif. Technol.* **2023**, *307*, 122794. [CrossRef]
64. Zhang, X.; Zhang, M.L.; Li, X.Y.; Xin, B.P.; Hao, J.; Li, J.Y.; Li, H.S.; Zhang, D.X.; Wu, X.Y.; Zhang, J.T. Charge reconstruction from simultaneous fe coordination and P/O co-doping in g-C_3N_4 for efficient photo-reductive recovery of uranium(VI). *Chem. Eng. J.* **2024**, *496*, 154319. [CrossRef]
65. Lu, Z.H.; Wang, Y.; Zhang, W.T.; He, T.; Wu, T.; Qiang, S.R.; Wang, J.J.; Li, P.; Liang, J.J.; Fan, Q.H. Enhanced electron delocalization in P doped g-C_3N_4 triggers U(VI) reduction. *Appl. Surf. Sci.* **2025**, *700*, 163278. [CrossRef]
66. Xie, J.Q.; Ji, D.Z.; Chang, Z.Y.; Wu, Y.H.; Lv, Q.Q.; Liu, X.K.; Shi, L. Synergy of P doping and crystallinity modulation in carbon nitride for enhancing photocatalytic uranyl reduction. *J. Colloid. Interf. Sci.* **2025**, *678*, 63–76. [CrossRef]
67. Chen, T.; Zhang, J.; Ge, H.L.; Li, M.X.; Li, Y.; Liu, B.; Duan, T.; He, R.; Zhu, W.K. Efficient extraction of uranium in organics-containing wastewater over g-C_3N_4/GO hybrid nanosheets with type-II band structure. *J. Hazard. Mater.* **2020**, *384*, 121383. [CrossRef]
68. Le, Z.G.; Xiong, C.B.; Gong, J.Y.; Wu, X.; Pan, T.; Chen, Z.S.; Xie, Z.B. Self-cleaning isotype g-C_3N_4 heterojunction for efficient photocatalytic reduction of hexavalent uranium under visible light. *Environ. Pollut.* **2020**, *260*, 114070. [CrossRef]
69. Zhang, Z.B.; Liu, C.; Dong, Z.M.; Dai, Y.; Xiong, G.X.; Liu, Y.H.; Wang, Y.Q. Synthesis of flower-like MoS_2/g-C_3N_4 nanosheet heterojunctions with enhanced photocatalytic reduction activity of uranium(VI). *Appl. Surf. Sci.* **2020**, *520*, 146352. [CrossRef]
70. Li, P.; Wang, J.J.; Wang, Y.; Dong, L.; Wang, W.; Geng, R.Y.; Ding, Z.; Luo, D.X.; Pan, D.Q.; Liang, J.J.; et al. Ultrafast recovery of aqueous uranium: Photocatalytic U(VI) reduction over CdS/g-C_3N_4. *Chem. Eng. J.* **2021**, *425*, 131552. [CrossRef]
71. Liu, C.; Dong, Z.M.; Yu, C.H.; Gong, Y.Y.; Wang, Y.Q.; Zhang, Z.B.; Liu, Y.H. Study on photocatalytic performance of hexagonal SnS_2/g-C_3N_4 nanosheets and its application to reduce U (VI) in sunlight. *Appl. Surf. Sci.* **2021**, *537*, 147754. [CrossRef]
72. Wu, F.; Zhang, Z.B.; Cheng, Z.P.; Zhou, R.Z.; Lin, Y.L.; Liu, Y.H.; Wang, Y.Q.; Cao, X.H.; Liu, M.G.; Liu, Y.H. The enhanced photocatalytic reduction of uranium(VI) by ZnS@g-C_3N_4 heterojunctions under sunlight. *J. Radioanal. Nucl. Chem.* **2021**, *329*, 1125–1133. [CrossRef]
73. Zhang, Z.B.; Zhou, R.Z.; Dong, Z.M.; Wu, Y.C.; Xu, L.; Xie, Y.H.; Li, Z.F.; Xiong, Y.T.; Wang, Y.Q.; Liu, Y.H. Visible-light induced photocatalytic removal of U(VI) from aqueous solution by MoS_2/g-C_3N_4 nanocomposites. *J. Radioanal. Nucl. Chem.* **2021**, *328*, 9–17. [CrossRef]
74. Le, Z.G.; Xue, J.M.; Wang, B.; Zhu, Y.A.; Wu, Z.W.; Nie, Y.D.; Xie, Z.B. MIL-100(Fe)/g-C_3N_4 composites with enhanced photocatalytic activity for UO_2^{2+} reduction under visible light. *Photochem. Photobiol. Sci.* **2023**, *22*, 59–71. [CrossRef]
75. Wang, F.; Liao, Y.; Li, T.T.; Xia, L.S. Coupling of CdS and g-C_3N_4 decorated dendritic fibrous nano-silica for efficient photocatalytic reduction of uranium (VI). *Sep. Purif. Technol.* **2022**, *299*, 121707. [CrossRef]
76. Wang, T.; Zhang, Z.B.B.; Dong, Z.M.; Cao, X.H.; Cheng, Z.P.; Liu, Y.H. A facile synthesis of g-C_3N_4/WS_2 heterojunctions with enhanced photocatalytic reduction activity of U(VI). *J. Radioanal. Nucl. Chem.* **2022**, *331*, 577–586. [CrossRef]
77. Liu, N.; Li, R.M.; Song, D.L.; Liu, Q.; Zhu, J.H.; Yu, J.; Li, Y.; Zhang, H.S.; Wang, J. Tubular LDHS@TCN composites for photo-assisted uranium extraction. *Prog. Nucl. Energ.* **2023**, *165*, 104910. [CrossRef]
78. Hou, G.L.; Dong, W.J.; Li, Z.F.; Cao, X.H.; Zou, L.X.; Liu, Y.H.; Zhang, Z.B. Donor-Acceptor characteristic g-C_3N_4 hollow nanospheres heterojunctions for efficient photocatalytic uranium reduction. *J. Solid State Chem.* **2024**, *336*, 124739. [CrossRef]
79. Li, Z.Z.; Li, Z.; He, F.; He, W.; Chen, Q.X.; Wang, H.Q. Synergistic enhancement of NC-GCN/Ag_2O photocatalytic reduction of uranium by D-A and p-n junction structures. *J. Mol. Liq.* **2024**, *409*, 125440. [CrossRef]

80. Kang, J.J.; Ouyang, J.L.; Yu, F.T.; Chen, Z.Y.; Song, F.R.; Liang, R.P.; Qiu, J.D. Molecular-level regulation strategies for charge separation in conjugated polymer/polymeric carbon nitride heterojunction enabling efficient uranium photoreduction. *J. Solid State Chem.* **2025**, *344*, 125173. [CrossRef]
81. Peng, W.; He, X.C.; Chen, X.L.; Zhang, Y.S.; Yan, C.P.; Chen, Z.S.; Hunga, G.L. Enhancement of U(VI) removal by g-C_3N_4/HAP composites via adsorption and solar driven photocatalysis synergy. *J. Water Process Eng.* **2025**, *72*, 107584. [CrossRef]
82. Song, Z.K.; Wang, B.; Qiu, J.L.; Nie, Y.D.; Li, P.; Zhu, Y.A.; Yan, C.P.; Xie, Z.B.; Chen, G.; Le, Z.G. Facile In-Situ synthesis of silicon Carbide-Graphitic carbon nitride composite for enhanced photocatalytic uranium (VI) recovery. *Appl. Surf. Sci.* **2025**, *684*, 161763. [CrossRef]
83. Xiao, Y.J.; Chen, S.; Li, P.; Zhang, D.; Wang, J.J.; Dong, H. Photocatalytic removal of U(VI) from aqueous solution under visible light by bismuth oxyiodide/graphitic carbon nitride composite. *J. Colloid Interface Sci.* **2025**, *684*, 131–139. [CrossRef]
84. Zhang, J.C.; Wang, Y.; Feng, L.J.; Zhang, J.; Tian, X.F.; Huang, S.H.; Yuan, Y.H.; Wang, N. Biochar decorated 2D/2D heterojunction with enhanced photocatalytic activity for uranium extraction. *Sep. Purif. Technol.* **2025**, *360*, 131026. [CrossRef]
85. Wang, W.; Luo, Q.; Li, L.Q.; Wang, Y.F.; Huo, X.B.; Chen, S.P.; Du, X.W.; Wang, N. Ni-single-atom mediated 2D heterostructures for highly efficient uranyl photoreduction. *Adv. Funct. Mater.* **2023**, *33*, 2302913. [CrossRef]
86. Hong, J.H.; Ma, R.; Wu, Y.C.; Wen, T.; Ai, Y.J. CoN_x/g-C_3N_4 Nanomaterials Preparation by MOFs Self-sacrificing Template Method for Efficient Photocatalytic Reduction of U(VI). *J. Inorg. Mater.* **2022**, *37*, 741. [CrossRef]
87. Huang, X.S.; Xioa, J.T.; Mei, P.; Wang, H.H.; Ishag, A.; Sun, Y.B. The synthesis of Z-scheme MoS_2/g-C_3N_4 heterojunction for enhanced visible-light-driven photoreduction of uranium. *Catal. Lett.* **2022**, *152*, 1981–1989. [CrossRef]
88. Li, S.T.; Wangh, Y.; Wang, J.J.; Liang, J.J.; Li, Y.Q.; Li, P. Modifying g-C_3N_4 with oxidized Ti_3C_2 MXene for boosting photocatalytic U(VI) reduction performance. *J. Mol. Liq.* **2022**, *346*, 117937. [CrossRef]
89. Mei, P.; Xiao, J.T.; Huang, X.S.; Ishag, A.; Sun, Y.B. Enhanced Photocatalytic Reduction of U(VI) on $SrTiO_3$/ g-C_3N_4 Composites: Synergistic Interaction. *Eur. J. Inorg. Chem.* **2022**, *2022*, e202101005. [CrossRef]
90. Zhang, X.Y.; Wang, J.J.; Li, P.; Tan, Z.Y.; Zeng, J.H.; He, Y.R.; Habibul, N. Removal of U(VI) from aqueous solution via photocatalytic reduction over WO_3/g-C_3N_4 composite under visible light. *Chem. Eng. J.* **2022**, *428*, 131209. [CrossRef]
91. Li, K.D.; Zheng, B.W.; Ding, L.; Tao, C.Y.; Zhang, S.; Zhang, L. Integration of high visible-light-driven ternary dual Z-scheme $AgVO_3$-$InVO_4$/g-C_3N_4 heterojunction nanocomposite for enhanced uranium(VI) photoreduction separation. *Environ. Pollut.* **2023**, *334*, 122168. [CrossRef]
92. Liu, J.X.; Wu, J.; Duan, Y.; Zhu, K.H.; Zheng, Z.H.; Wang, J.S. Efficient removal of U(VI) from aqueous solution by CNN/UiO-66 under simulated sunlight irradiation: The synergy of adsorption and photocatalysis. *Environ. Sci. Pollut. Res.* **2024**, *31*, 20999–21011. [CrossRef]
93. Wen, Y.; Sun, Y.C.; Liu, Y.T.; Zhao, M.; Zhao, L.S. Green synthesis of 2% g-C_3N_4/SnS_2-V_3/CQD1 composite photocatalyst from waste plant soot for efficient U(VI) removal: Mechanistic insights. *Chem. Eng. J.* **2024**, *494*, 153247. [CrossRef]
94. Li, K.D.; Xiong, T.; He, Z.B.; Zhang, L. Efficient assembly of a rare earth-indium bimetallic vanadate/ g-C_3N_4 heterojunction for enhanced uranium(VI) visible-light photocatalytic separation. *Langmuir* **2025**, *41*, 18682–18693. [CrossRef]
95. Qiu, J.L.; Zhu, Y.A.; Wang, B.; Nie, Y.D.; Song, Z.K.; Li, P.; Xie, Z.B.; Le, Z.G. Enhanced removal of aqueous uranium: Photocatalytic U(VI) reduction over bismuth vanadate/hydrothermal carbon nitride under visible light. *J. Environ. Chem. Eng.* **2025**, *13*, 115009. [CrossRef]
96. Xiao, Y.J.; Chen, S.; Li, P.; Zhang, D.; Wang, J.J.; Dong, H.; He, Y.R. Bismuth tungstate/graphite carbon nitride composites for efficient photocatalytic reduction of U(VI): Synthesis, performance, and mechanism. *J. Environ. Chem. Eng.* **2025**, *13*, 116654. [CrossRef]
97. Zhu, Y.A.; Nie, Y.D.; Qiu, J.L.; Zhu, X.; Song, Z.K.; Wang, B.; Xie, Z.B.; Le, Z.G. Photocatalytic reduction of uranium over a novel Z-scheme Ni-MOF/g-C_3N_4 heterojunction. *Appl. Surf. Sci.* **2025**, *709*, 163791. [CrossRef]
98. Li, S.Y.; Yang, X.Y.; Cui, Z.P.; Xu, Y.; Niu, Z.W.; Li, P.; Pan, D.Q.; Wu, W.S. Efficient photoreduction strategy for uranium immobilization based on graphite carbon nitride/perovskite oxide heterojunction nanocomposites. *Appl. Catal. B-Environ. Energy* **2021**, *298*, 120625. [CrossRef]
99. Li, Z.F.; Zhang, Z.B.; Dong, Z.M.; Wu, Y.C.; Liu, J.Y.; Cheng, Z.P.; Liu, Y.H.; Wang, Y.C.; Zheng, Z.J.; Cao, X.H.; et al. Synthesis of MoS_2/P-g-C_3N_4 nanocomposites with enhanced visible-light photocatalytic activity for the removal of uranium (VI). *J. Solid State Chem.* **2021**, *302*, 122305. [CrossRef]
100. Dai, Z.R.; Zhao, S.; Lian, J.J.; Li, L.; Ding, D.X. Efficient visible-light-driven photoreduction of U(VI) by carbon dots modified porous g-C_3N_4. *Sep. Purif. Technol.* **2022**, *298*, 121590. [CrossRef]
101. Hong, J.H.; Ma, R.; Wu, Y.C.; Liu, Y.; Wen, T.; Zhang, S.; Wang, S.H.; Wang, X.K.; Ai, Y.J. Experimental and theoretical identifications of durable Fe–Nx configurations embedded in graphitic carbon nitride for uranium photoreduction. *J. Environ. Chem. Eng.* **2022**, *10*, 108374. [CrossRef]
102. Li, H.P.; Qing, Q.; Zheng, L.Y.; Xie, L.; Gan, Z.Q.; Huang, L.Q.; Liu, S.; Wang, Z.; Lu, Y.X.; Chen, J. Carbon dots and carbon nitride composite for photocatalytic removal of uranium under air atmosphere. *Chin. Chem. Lett.* **2022**, *33*, 3573–3576. [CrossRef]

103. Liu, J.Y.; Zhang, Z.B.; Dong, Z.M.; Zhu, X.; Gao, D.L.; Cheng, Z.P.; Cao, X.H.; Wang, Y.Q.; Liu, Y.H. Metal-free CQDs introduced g-C_3N_4 nanosheets with enhanced photocatalytic reduction performance of uranium (VI). *J. Radioanal. Nucl. Chem.* **2022**, *33*, 2093–2104. [CrossRef]
104. Xue, J.M.; Xie, Z.B.; Wang, B.; Zhu, Y.A.; Wu, Z.W.; Nie, Y.D.; Le, Z.G. Enhanced visible-light photocatalytic performance by PPy/CN composites for reduction of UO_2^{2+}. *J. Solid State Chem.* **2022**, *315*, 123440. [CrossRef]
105. Zheng, Z.J.; Wang, X.Z.; Ye, Z.F.; Jin, R.; Qiu, H.W.; Chen, J.J.; Wang, Y.Q.; Dong, Z.M.; Zhang, Z.B.; Liu, Y.H. In situ growth $ZnIn_2S_4$ nanosheets on g-C_3N_4 nanorods with boosted charge transfer for high-efficient photocatalysis removal of U(VI). *Sep. Purif. Technol.* **2025**, *364*, 132271. [CrossRef]
106. Dai, Z.R.; Chen, L.J.; Zhang, W.L.; Liang, B.; Gao, Y.; Li, L. K doped defective g-C_3N_4 decorated with cyano group for boosting visible-light driven photocatalytic removal of uranium. *Sep. Purif. Technol.* **2024**, *338*, 126537. [CrossRef]
107. Chen, Q.X.; Xiao, Q.X.; HHe, F.; He, W.; Liu, K.K.; Zhao, C.K.; Chang, Z.Y.; Wang, H.Q. Synergetic dual co-catalyst and interfacial bonds in N-CQDs/NCN/BNQDs to promote photoremoval of uranium(VI). *Sep. Purif. Technol.* **2025**, *363*, 132193. [CrossRef]
108. Wang, Y.G.; Zhang, L.; Liang, R.P.; Qiu, J.D. Dual vacancies synergistically induced hybridization effect of $Ti_3C_2T_x$-based photocatalyst for enhanced U(VI) photoreduction. *Sep. Purif. Technol.* **2025**, *354*, 128664. [CrossRef]
109. Gao, H.H.; Xu, J.Z.; Zhou, J.T.; Zhang, S.W.; Zhou, R. Metal organic framework derived heteroatoms and cyano (-C≡N) group co-decorated porous g-C_3N_4 nanosheets for improved photocatalytic H_2 evolution and uranium(VI) reduction. *J. Colloid Interf. Sci.* **2020**, *570*, 125–134. [CrossRef] [PubMed]
110. Hu, E.M.; Chen, Q.; Gao, Q.; Fan, X.F.; Luo, X.J.; Wei, Y.; Wu, G.; Deng, H.B.; Xu, S.C.; Wang, P.; et al. Cyano-functionalized graphitic carbon nitride with adsorption and photoreduction isosite achieving efficient uranium extraction from seawater. *Adv. Funct. Mater.* **2024**, *34*, 2312215. [CrossRef]
111. Li, Q.; Wang, J.Q.; Hou, H.R.; Wang, M.; Yu, S.J.; Xu, H.; Fu, D.; Wang, X.X. Efficient uranium removal by amidoxime functionalized graphitic carbon nitride and its potential mechanism. *J. Radioanal. Nucl. Chem.* **2025**, *334*, 419–431. [CrossRef]
112. Wang, P.; Hu, E.M.; Wu, L.Z.; He, J.H.; Wang, Y.H.; Ou, Z.H.; Yang, F.; Chen, T.; Zhu, W.K. Tailoring the electronic microenvironment of polymeric carbon nitride to accelerate reduction crystallization kinetics of uranium extraction from seawater. *Appl. Catal. B-Environ. Energy* **2025**, *371*, 125266. [CrossRef]
113. Zhu, J.H.; Hao, X.; Liu, Q.; Liu, J.Y.; Chen, R.R.; Yu, J.; Li, R.M.; Liu, P.L.; Wang, J. Exploring the application of amino functionalized three-dimensional macroscopic g-C_3N_4 sponge for enhanced uranium recovery. *J. Mol. Liq.* **2021**, *343*, 117238. [CrossRef]
114. Momin, Z.H.; Lingamdinne, P.L.; Kulkarni, R.; Pal, A.C.; Choi, Y.L.; Chang, Y.Y.; Koduru, J.R. Exploring recyclable alginate-enhanced GCN-LDO sponge for U(VI) and Cd(II) removal: Insights from batch and column studies. *J. Hazard. Mater.* **2024**, *469*, 134015. [CrossRef] [PubMed]
115. Lingamdinne, L.P.; Kulkarni, R.; Reddy, N.S.; Chang, Y.Y.; Koduru, J.R. Efficient preparation and characterization of LDH/GCN based 3D foam for sustainable continuous column removal of U^{6+} and Cd^{2+} from water: Mechanistic insights and application feasibility. *Environ. Sci. Water Res. Technol.* **2025**, *11*, 1668–1680. [CrossRef]
116. Zhou, Q.; Jin, B.; Zhao, P.; Chu, S.J.; Peng, R.F. rGO/CNQDs/ZIF-67 composite aerogel for efficient extraction of uranium in wastewater. *Chem. Eng. J.* **2021**, *419*, 129622. [CrossRef]
117. Qin, S.L.; Sha, J.N.; Yang, P.P.; Li, S.W.; Liu, C.T.; Shen, C.Y. Graphene oxide/graphitic carbon nitride/polyamide oxime nanofibers for adsorption and photocatalytic reduction of uranium from seawater. *Inorg. Chem. Front.* **2024**, *11*, 6156–6167. [CrossRef]
118. Yu, J.Q.; Zhang, H.S.; Liu, Q.; Yu, J.; Zhu, J.H.; Li, R.H.; Liu, P.L.; Li, Y.; Wang, J. Antibacterial AO-CS/CdS-porous few-layer g-C_3N_4 nanofiber membrane for high-efficiency uranium extraction from seawater: A dual adsorption-photocatalytic regulation strategy. *Chem. Eng. J.* **2023**, *471*, 144705. [CrossRef]

Disclaimer/Publisher's Note: The statements, opinions and data contained in all publications are solely those of the individual author(s) and contributor(s) and not of MDPI and/or the editor(s). MDPI and/or the editor(s) disclaim responsibility for any injury to people or property resulting from any ideas, methods, instructions or products referred to in the content.